



Cloud processing of DMS oxidation products limits SO₂ and OCS production in the Eastern North Atlantic marine boundary layer

Delaney B. Kilgour¹, Christopher M. Jernigan^{1,*,#}, Olga Garmash^{2,^}, Sneha Aggarwal^{3,4}, Claudia Mohr^{3,†,+}, Matt E. Salter^{3,4}, Joel A. Thornton², Jian Wang⁵, Paul Zieger^{3,4}, Timothy H. Bertram¹

5 ¹Department of Chemistry, University of Wisconsin-Madison, Madison, WI 53706, USA

²Department of Atmospheric Sciences, University of Washington, Seattle, WA 98195, USA

³Department of Environmental Science, Stockholm University, Stockholm, 10691, Sweden

⁴Bolin Centre for Climate Research, Stockholm University, Stockholm, 10691, Sweden

10 ⁵Center for Aerosol Science and Engineering, Department of Energy, Environmental and Chemical Engineering, Washington University in St. Louis, St. Louis, MO 63130, USA

*Now at Cooperative Institute for Research in Environmental Sciences, University of Colorado, Boulder, CO 80305, USA

#Now at NOAA Chemical Sciences Laboratory, Boulder, CO 80305, USA

[^]Now at Department of Chemistry, University of Copenhagen, DK-2100 Copenhagen Ø, Denmark

[†]Now at Department of Environmental Systems Science, ETH Zurich, 8092 Zürich, Switzerland

15 ⁺Now at Laboratory of Atmospheric Chemistry, Paul Scherrer Institute, 5232 Villigen, Switzerland

Correspondence to: Timothy H. Bertram (timothy.bertram@wisc.edu)

Abstract. Dimethyl sulfide (DMS) is the major sulfur species emitted from the ocean. The gas-phase oxidation of DMS by hydroxyl radicals proceeds through the stable, soluble intermediate hydroperoxymethyl thioformate (HPMTF), eventually forming carbonyl sulfide (OCS) and sulfur dioxide (SO₂). Recent work has shown that HPMTF is efficiently lost to marine boundary layer (MBL) clouds, thus arresting OCS and SO₂ production and their contributions to new particle formation and growth events. To date, no long-term field studies exist to assess the extent to which frequent cloud processing impacts the fate of HPMTF. Here we present six weeks of measurements of cloud fraction and the marine sulfur species, methanethiol, DMS, and HPMTF, made at the ARM Research Facility on Graciosa Island, Azores, Portugal. Using an observationally constrained chemical box model, we determine that cloud loss is the dominant sink of HPMTF in this region of the MBL during the study, accounting for 79-91% of HPMTF loss on average. When accounting for HPMTF uptake to clouds, we calculate a campaign average reduction in DMS-derived MBL SO₂ and OCS of 52-60% and 80-92% for the study period. Using yearly measurements of site- and satellite-measured 3-dimensional cloud fraction and DMS climatology, we infer that HPMTF cloud loss is the dominant sink of HPMTF in the Eastern North Atlantic during all seasons, and occurs on timescales faster than what is prescribed in global chemical transport models. Accurately resolving this rapid loss of HPMTF to cloud has important implications for constraining drivers of MBL new particle formation.

20
25
30

1 Introduction

Aqueous reactions in clouds can significantly alter trace gas and aerosol budgets by acting as efficient, terminal sinks for water-soluble species and sites for the formation of reactive products (Barth et al., 2021; Li et al., 2017; Yang et al., 2015).



35 Examples include cloud scavenging of dinitrogen pentoxide (N_2O_5) and nitric acid (HNO_3) influencing the tropospheric NO_x budget (Holmes et al., 2019; Levine and Schwartz, 1982), uptake of sulfur dioxide (SO_2) contributing to aerosol production and acid rain (Irwin and Williams, 1988), cloud processing increasing the production of isoprene secondary organic aerosol (SOA) (Lamkaddam et al., 2021), and cloud chemistry controlling the conversion of dimethyl sulfide (CH_3SCH_3 ; DMS) to SO_2 and methane sulfonic acid ($\text{CH}_3\text{SO}_3\text{H}$; MSA) (Chen et al., 2018; Hoffmann et al., 2016). By redistributing chemical budgets in the lower troposphere, cloud processing can consequently affect the spatial distribution and availability of vapors
40 to contribute to new particle formation (Novak et al., 2021), the concentration of cloud condensation nuclei (CCN) (Feingold et al., 1998), and the magnitude of long-lived climate forcing products (Jernigan et al., 2022a; Novak et al., 2021).

For water-soluble species with high uptake coefficients that react irreversibly, uptake to cloud droplets is limited by gas-phase diffusion to the droplet surface, leading to in-cloud lifetimes for typical cloud conditions on the order of ten seconds or less
45 (Holmes et al., 2019; Levine and Schwartz, 1982). Large eddy simulation studies indicate the residence time of air within the cloud is significantly longer, ranging from 15 minutes to two hours for many stratus and stratocumulus clouds (Feingold et al., 1998, 2013; Kogan, 2006; Stevens et al., 1996), and even longer for cirrus clouds (Podglajen et al., 2016). This results in the complete and rapid removal of water-soluble molecules that react irreversibly in the cloud layer. As such, cloud processing of water-soluble species with irreversible uptake in the well-mixed boundary layer is dependent on the mixing rate of clear air
50 into cloud, here referred to as the cloud entrainment rate (Holmes et al., 2019). A new method using entrainment-limited uptake, incorporating grid cell cloud fraction from satellite reanalysis products (MERRA-2) and entrainment into the kinetic rate expression, was recently developed to account for cloud uptake (Holmes, 2022; Holmes et al., 2019), and has been implemented into global chemical transport models to evaluate chemical budgets for a variety of species, including halogen, sulfur, and nitrogen-containing molecules (Alexander et al., 2020; Chan et al., 2021; Holmes et al., 2019; Jernigan et al., 2022a;
55 Novak et al., 2021; Shah et al., 2021; Wang et al., 2021). This method utilizes an average entrainment rate of 1 h^{-1} based on mean values of cloud residence time for stratus and stratocumulus clouds scaled by satellite-derived 3D cloud fraction (Holmes et al., 2019). This entrainment-limited method has been shown to be more physically accurate and less computationally expensive than previous parameterizations for cloud uptake, such as the thin cloud (Parrella et al., 2012) and cloud partitioning (Tost et al., 2006) approximations.

60

Trace gas uptake by clouds can play a particularly important role in trace gas and aerosol budgets in the marine boundary layer (MBL) due to the large and persistent cover of low-level clouds over the oceans. Globally, stratus and stratocumulus clouds are present over 10-70% of the MBL, and their coverage can exceed 50% in the annual mean over subtropical and midlatitude oceans (Wood, 2012). More recent estimates reported five-year averaged low-level cloud fractions even larger, exceeding 70%
65 in the subtropics and the extratropical North Atlantic, North Pacific, and Southern Oceans, regions where stratocumulus cloud decks are common (Naud et al., 2023). Given the ocean is the largest natural source of reduced sulfur to the atmosphere, primarily in the form of DMS ($\sim 27.1 \text{ Tg S yr}^{-1}$) (Andreae, 1990; Bates et al., 1992; Hulswar et al., 2022) and to a lesser extent,

methanethiol (CH_3SH ; MeSH) (Novak et al., 2022), low-level MBL clouds have the potential to impact the sulfur budget globally through the uptake of their soluble oxidation intermediates.

70

DMS is formed in the ocean as one of two major degradation products of the precursor algal metabolite dimethylsulfoniopropionate (DMSP) (Challenger and Simpson, 1948). The other DMSP degradation product is MeSH (Kiene, 1996). Once emitted to the atmosphere, the primary fate of both DMS and MeSH is reaction with hydroxyl radicals (OH), with the lifetime of DMS to OH approximately five times longer than that of MeSH to OH at 298 K (Burkholder et al., 2019). The OH-oxidation of MeSH and subsequent O_2 addition forms the CH_3SO_2 radical, which has a temperature-dependent branching ratio forming SO_2 or MSA (Chen et al., 2023). Recent computational work has shown the SO_2 yield from CH_3SO_2 is 99% at 300 K, but drops to 4% at 260 K (Chen et al., 2023). The OH-oxidation of DMS is also highly temperature-dependent, proceeding either by OH-addition (~30% at 298 K) or by H-abstraction (~70% at 298 K). The OH-addition pathway leads to the formation of several soluble products, including MSA, methane sulfinic acid ($\text{CH}_4\text{O}_2\text{S}$; MSIA), dimethyl sulfoxide (75 CH_3SOCH_3 ; DMSO), and dimethyl sulfone ($\text{C}_2\text{H}_6\text{O}_2\text{S}$; DMSO_2), and primarily contributes to particle growth (Barnes et al., 1994; Conley et al., 2009; Hoffmann et al., 2016). The H-abstraction pathway produces the methylthiomethyl peroxy radical ($\text{CH}_3\text{SCH}_2\text{OO}$; MTMP), which can undergo intramolecular hydrogen shift rearrangements and additions of O_2 to form the stable, soluble intermediate hydroperoxymethyl thioformate ($\text{HOOCH}_2\text{SCHO}$; HPMTF) (Berndt et al., 2019; Wu et al., 2015). This isomerization pathway to HPMTF production competes with bimolecular reactions between MTMP and NO, HO_2 , and 85 RO_2 (Berndt et al., 2019), which are typically in low concentration in the marine atmosphere (<15 ppt, <15 ppt, and <150 ppt, respectively) (Creasey et al., 2003; Lee et al., 2009; Vaughan et al., 2012). Once formed, HPMTF is further oxidized by OH to carbonyl sulfide (OCS) (Jernigan et al., 2022a) and SO_2 (Veres et al., 2020), leading to new sulfate (SO_4^{2-}) aerosol particle formation through the production of sulfuric acid (H_2SO_4). Recent aircraft measurements found HPMTF was globally ubiquitous in the MBL (Veres et al., 2020) and global chemical transport modeling showed it is the dominant reservoir of 90 DMS oxidation products; analyses in this study indicated the yield of HPMTF from the DMS H-abstraction pathway (α_{HPMTF}) was 0.76, and estimated 46% of all emitted DMS globally formed HPMTF (Novak et al., 2021). HPMTF has also been shown to be efficiently depleted in MBL cloud suggesting irreversible loss (Novak et al., 2021; Siegel et al., 2023; Veres et al., 2020; Vermeuel et al., 2020), which is briefly summarized below.

95 Aircraft measurements by Veres et al. (2020) first showed the rapid depletion of HPMTF within the MBL cloud layer during ATom 3 and ATom 4, reporting on average a 75% reduction in HPMTF in the presence of cloud. This result was subsequently supported by several qualitative findings at ground sites. For example, in coastal Southern California, Vermeuel et al. (2020) found that observed HPMTF diurnal profiles could only be reproduced by a model when including a time-dependent HPMTF cloud loss based on GOES imagery. In the Arctic, Siegel et al. (2023) measured reduced HPMTF in cloudy and semi-cloudy 100 conditions compared to cloud-free conditions. The only existing collocated measurements of DMS and HPMTF are from a flight off the coast of Southern California (Novak et al., 2021). In cloud-free conditions, average $[\text{DMS}]/[\text{HPMTF}]$ was low



(1.25), but was much higher (20) below the cloud deck, evidence for cloud processing of the DMS-oxidation product, HPMTF. Analysis of eddy covariance flux measurements of HPMTF on this same flight produced the only quantified loss rate of HPMTF to cloud currently in the literature (Novak et al., 2021). The timescale of HPMTF loss to a stratocumulus cloud deck was 1.2 ± 0.6 h, which was greater than four times faster than other HPMTF loss pathways. This irreversible cloud uptake of HPMTF weakens the links between DMS and the climate forcing products OCS and SO₂ along the H-abstraction pathway, and subsequent new particle formation and CCN production. Global model analyses incorporating the HPMTF cloud loss term determined from Novak et al. (2021) indicated cloud chemistry reduced SO₂ production from DMS globally by 35% (Novak et al., 2021) and OCS production globally by 92% (Jernigan et al., 2022a). Further, the prompt conversion of aqueous HPMTF in cloud to SO₄²⁻ at unit yield (Jernigan et al., 2024) could significantly increase SO₄²⁻ concentrations while bypassing new particle formation (Novak et al., 2021).

However, to date, no long-term field studies exist with coincident measurements of DMS and HPMTF. This limits our ability to assess how cloud chemistry impacts DMS oxidation on long time scales, where cloud fraction and cloud type are expected to vary. Here we present six weeks of *in situ* measurements of the reactant and product pair DMS and HPMTF, and MeSH, made in the Eastern North Atlantic (ENA). We use these gas-phase measurements and extensive observations of atmospheric and cloud properties made at the Atmospheric Radiation Measurement (ARM) Research Facility on Graciosa Island, Azores, Portugal, with a chemical box model to determine how frequent cloud processing impacts the conversion of DMS to SO₂ and OCS in the MBL. We show that over a six-week period, cloud uptake is the dominant loss process of HPMTF and occurs at rates significantly faster than what is currently prescribed in global chemical transport models where uptake is scaled by satellite-derived cloud fraction.

2 Methods

2.1 Measurements of gas-phase sulfur species at ENA

Continuous, real-time measurements of DMS, MeSH, and HPMTF were made from June 1, 2022 to July 15, 2022 at the ENA ARM Research Facility on Graciosa Island, Azores, Portugal (39.0916 °N, 28.0257 °W, 30 m elevation) as part of the Aerosol Growth in the Eastern North Atlantic (AGENA) project. DMS and MeSH were measured at 10 m above ground level with a Vocus proton transfer reaction time-of-flight mass spectrometer (RT-Vocus; Aerodyne Research, Inc. and ToFwerk AG) (Krechmer et al., 2018). Full details of the RT-Vocus sampling at AGENA and quantifications of DMS and MeSH are reported in Kilgour et al. (2024). Collocated HPMTF measurements at 4 m above ground level were made with a chemical ionization time-of-flight mass spectrometer (Aerodyne Research, Inc. and ToFwerk AG) equipped with a medium-pressure (50 mbar) Vocus AIM reactor (Riva et al., 2024). Multiple reagent ions, namely iodide, bromide, and benzene, were generated using VUV lamps to target a wide range of oxygenated and non-oxygenated compounds. HPMTF was detected with the iodide reagent ion as an adduct ion with iodide ([I•C₂H₄O₃S]⁻). This mass was <0.1 m/Q from N₂O₅, and at the same unit mass as



several other peaks (Supplemental S1). The instrument resolution ($m/\Delta m = 5500$) did not enable separable peak fitting of the
135 closest two peaks, HPMTF and N_2O_5 , leading to some early morning interference in HPMTF when N_2O_5 was present. However,
the N_2O_5 signal was small due to low NO_x ambient conditions, and HPMTF and N_2O_5 had different diurnal profiles, resulting
in minimal impact overall for this analysis. Vocus AIM zeros were completed every hour at the capillary, and HPMTF was
quantified post-campaign with the experimentally-determined humidity-dependent calibration factor for formic acid based on
the similar iodide adduct binding enthalpies for HPMTF and formic acid (Iyer et al., 2016; Jernigan et al., 2022a). By
140 comparing clear sky measurements of HPMTF to modelled clear sky HPMTF, we estimate HPMTF concentrations reported
here, using the formic acid calibration factor, are underestimated by up to 60% due to a combination of inlet loss of HPMTF
and lack of an authentic calibration standard (Fig. S1). As a result, all of the following reported measurements of [HPMTF]
and [DMS]/[HPMTF], which use the calibration factor to formic acid, should be interpreted as a lower limit and upper limit,
respectively. More details on the HPMTF measurement, quantification, and derivation of its uncertainty are in Supplemental
145 S1. Limits of detection for a signal-to-noise ratio of 3 at 5-minute averaging for DMS, MeSH, and HPMTF were 1.8, 5.1, and
0.1 ppt, respectively (Bertram et al., 2011). HPMTF was below the detection limit in 19% of 5-minute averaged HPMTF data
points; diurnally, this was largest in the early morning at Hour 7 (32%) and lowest in the afternoon at Hour 16 (3.6%), where
these and the following hours are in local time. Points below the detection limit were replaced with half the detection limit for
reporting statistics and interpreting [DMS]/[HPMTF] ratios (Antweiler and Taylor, 2008). Since the subsequent analysis
150 utilizes afternoon [DMS]/[HPMTF] ratios, the treatment of the detection limit had a minimal effect relative to all other sources
of uncertainty. Lastly, DMS, MeSH, and HPMTF were insensitive to nearby Graciosa airport activity and so no pollution flag
was applied to the measurements in this work, contrary to those in Kilgour et al. (2024).

2.2 Development of a box model to derive HPMTF cloud loss rates from [DMS]/[HPMTF]

A coupled ocean-atmosphere 0-D chemical box model was created in the Framework for 0-D Atmospheric Modeling (F0AM,
155 Wolfe et al., 2016), implementing the Master Chemical Mechanism (MCM) v3.3.1 (<http://mcm.york.ac.uk>) (last access: 5 Dec
2023) (Jenkin et al., 1997; Saunders et al., 2003), and updated sulfur chemistry for MeSH, HPMTF, and other DMS oxidation
products. The constrained box model was used to determine the rate of HPMTF lost to cloud as discussed below.

The box model was run with a four-day spin-up period to allow reactive intermediates to reach equilibrium. Diurnally-averaged
160 measurements from the Aerosol Observing System (AOS) (Uin et al., 2019) and RT-Vocus during the study period were used
as inputs to constrain pressure, temperature, humidity, and trace gas concentrations (O_3 , CO, VOC). The emission flux of DMS
(4.5×10^9 molec. $cm^{-2} s^{-1}$) was prescribed to match the observed study diurnal-average mixing ratio (diurnal minimum 80 ppt
– diurnal maximum 137 ppt) and was within the range of typical oceanic DMS emission fluxes ($0-7.0 \times 10^9$ molec. $cm^{-2} s^{-1}$)
(Hulswar et al., 2022). A constant OH profile peaking at 4.5×10^6 molec. cm^{-3} (diurnal average of 1.3×10^6 molec. cm^{-3}) was
165 used. This OH profile agreed well with previous predictions of the zonally averaged surface OH concentration for July at this
latitude of 1.49×10^6 molec. cm^{-3} (Spivakovsky et al., 2000). This OH concentration from climatological analysis was



determined in a photochemical model constrained by surface and column observations of variables affecting OH, such as the concentrations of O₃, water vapor, nitrogen oxides, CO, hydrocarbons, and temperature and cloud optical depth (Spivakovsky et al., 2000). OH production below and above cloud was assumed to be approximately equivalent, based on the following two pieces of evidence: (1) <15% difference in measured $J(\text{O}^1\text{D})$ in cloudy and clear conditions in the North Pacific during ATom (Hall et al., 2018), and (2) given DMS and MeSH are co-emitted species with different, known OH loss rates, $[\text{DMS}]/[\text{MeSH}]$ can provide insight into OH exposure. Our measurements indicate no dependence in measured midday $[\text{DMS}]/[\text{MeSH}]$ on cloud fraction (Fig. S2). As a result, the model used a constant OH profile, independent of cloud fraction, to interpret cloud loss of HPMTF across the study. Based on average boundary layer heights determined from sonde profiles approximately every 12 hours during the study (average 1009 ± 312 m (1σ) and interquartile range 748 – 1240 m), a static boundary layer height of 1000 m was assumed. Free troposphere – boundary layer mixing was treated as a first order dilution term, calculated using an exchange velocity of 0.5 cm s^{-1} (Faloona, 2009) and a 1000 m boundary layer height. Additional discussion on the dependence of boundary layer height and exchange velocity on the fraction of DMS oxidized in the MBL can be found in Section 3.2.1.

In the model, HPMTF was formed chemically via the temperature-dependent isomerization of MTMP (Assaf et al., 2023) and lost via OH-oxidation (Jernigan et al., 2022a), dry deposition (Vermeuel et al., 2020), aerosol uptake (Jernigan et al., 2022b), and a variable fourth term, interpreted as cloud loss. HPMTF OH-oxidation was set to $1.4 \times 10^{-11} \text{ cm}^3 \text{ molec.}^{-1} \text{ s}^{-1}$ forming SO₂ at 87% yield and OCS at 13% yield (Jernigan et al., 2022a), HPMTF dry deposition was set to 0.75 cm s^{-1} and was independent of wind speed over the range of wind speeds observed (Vermeuel et al., 2020), and uptake to marine aerosol particles was calculated according to Eq. 1, where A is the aerosol surface area density, D_g is the diffusivity in air, r is the aerosol radius, v is the mean molecular speed, and γ is the reactive uptake coefficient. A constant aerosol surface area of $45.0 \mu\text{m}^2 \text{ cm}^{-3}$ was used, corresponding to the median dry aerosol surface area measured by a scanning mobility particle sizer (measures 10 nm – 1000 nm diameter particles) during the six week study ($20.0 \mu\text{m}^2 \text{ cm}^{-3}$ and 12.6-25.3 $\mu\text{m}^2 \text{ cm}^{-3}$ interquartile range) with an estimated hygroscopic growth factor of 1.5 applied (Zhang et al., 2014). The reactive uptake coefficient, γ , was set to 0.0016, corresponding to an experimentally-measured value for deliquesced NaCl particles (Jernigan et al., 2022b). Aerosol uptake (De Bruyn et al., 1994; Hoffmann et al., 2021) and dry deposition equivalent to the HPMTF dry deposition (Johnson, 2010; Vermeuel et al., 2020) was also included for the DMS oxidation products MSIA, MSA, DMSO, and DMSO₂, but the model did not treat cloud loss of these species. A complete table of updated model chemical reactions relevant to DMS, MeSH, and HPMTF is included in Table S1.

$$k = A \left(\frac{r}{D_g} + \frac{4}{v\gamma} \right)^{-1} \quad (1)$$



The difference between the clear sky modelled [DMS]/[HPMTF] diurnal profile and measurements of [DMS]/[HPMTF] diurnal profiles during the study were used to assign a fourth term, interpreted as the rate of HPMTF cloud loss. This was completed for the 31 study days with at least 20% data coverage in Hours 14-15 and at least 25% data coverage in Hours 13-17. These thresholds were selected to ensure data coverage when the diurnal profile of [DMS]/[HPMTF] was at a stable minimum. Since measured [DMS]/[HPMTF] is an upper limit, as discussed in Section 2.1, the derived cloud loss rates from residual [DMS]/[HPMTF] should also be interpreted as an upper limit. This same analysis was completed with [HPMTF] corrected so clear sky measurements of HPMTF agreed with clear sky modelled HPMTF (Fig. S1). From this analysis, we estimate cloud loss terms of HPMTF are an overestimate by up to a factor of three. Loss rates of HPMTF to cloud and the fractional loss of HPMTF to individual pathways below are reported as ranges based on this uncertainty to more accurately compare to literature values. More details on derivation of cloud loss terms are in Section 3.2.2.

2.3 Supporting measurements

Continuous measurements at ENA provided by ARM were used in tandem with DMS, MeSH, and HPMTF measurements to evaluate trends in HPMTF cloud loss rates. Best estimates of cloud base height (CBH) were determined from ceilometer and micropulse lidar measurements saved at 1 Hz (Johnson et al., 2022). Boundary layer heights (BLH) for the study period were determined manually based on inflection points in potential temperature and water mixing ratio (Albrecht et al., 1995) in sonde measurements launched two to three times per day (Riihimaki et al., 2022). Well-mixed boundary layers had vertical slopes in both potential temperature and mixing ratio below the inversion layer. For the yearlong analysis, BLHs were determined using the Heffter algorithm (Heffter, 1980), as these BLHs agreed with sonde measurements during the study, are independent of cloudiness, and have been used for analysis at this site previously (Ghate et al., 2023). Site-measured horizontal cloud fractions (CF_H) were determined from the percentage of opaque pixels in total sky imager hemispheric sky images recorded every minute during daylight hours and when solar elevation was above 10° (Flynn and Morris, 2022). Site-measured vertical cloud fractions (CF_V) and 3-dimensional cloud fractions (CF_{3A}) were calculated according to Eq. 2 and 3, respectively. For this calculation, sonde-derived BLHs were linearly interpolated to match the time points of CBH measurements, resulting in CF_V uncertainty largely dependent on assignment of BLH. This calculation assumed the vertical distance between the detected CBH and BLH was fully filled with cloud, such that the cloud horizontal depth in CF_H does not impact the calculation.

$$CF_V = \frac{BLH - CBH}{BLH} \quad (2)$$

$$CF_{3A} = CF_H \times CF_V \quad (3)$$

CF_{3A} was compared to 3-dimensional cloud fraction derived from MERRA-2 (Modern-Era Retrospective Reanalysis for Research and Applications, Version 2) (Gelaro et al., 2017) (CF_{3M}), which resolves cloud properties and cloud fraction ($CF_{VerticalLayer}$) at $0.5^\circ \times 0.625^\circ$ resolution for 42 vertical pressure-resolved layers ($\Delta P_{VerticalLayer}$) every three hours. CF_{3M} was



235 calculated as a weighted average cloud fraction (Eq. 4) over the entire boundary layer ($\Delta P_{\text{BoundaryLayer}}$) for a $4^\circ \times 5.625^\circ$ region encompassing Graciosa Island (coordinates $37\text{--}41^\circ \text{N}$ and $30.625\text{--}25^\circ \text{W}$). Boundary layers used for calculation were again based on the Heffter algorithm for sonde measurements (Riihimaki et al., 2022) and linearly interpolated to match MERRA-2 time points. These latitude, longitude, and boundary layer constraints were chosen to align with the inputs into the global chemical transport model, GEOS-Chem, if one were to model the impact of cloud chemistry in this region (Holmes et al., 2019).

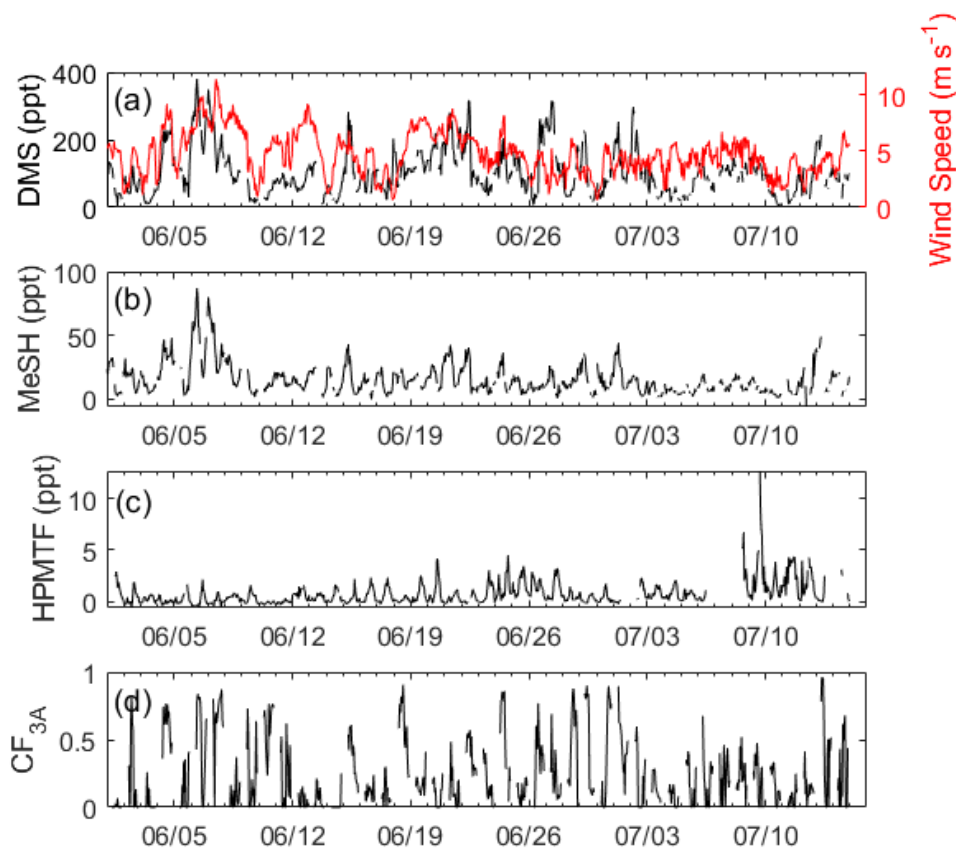
$$CF_{3M} = \frac{CF_{\text{VerticalLayer}} \times \Delta P_{\text{VerticalLayer}}}{\Delta P_{\text{Boundary Layer}}} \quad (4)$$

3 Results

240 3.1 Cloud and gas-phase sulfur measurements at ENA

The time series of DMS, MeSH, HPMTF, and CF_{3A} are shown in Fig. 1. DMS showed large variability throughout the study, mostly driven by wind speed, and averaged 106 ± 69 ppt. Here and in the following reported measurements of gas-phase concentrations and gas-phase ratios, standard deviations reflect natural variability in ambient concentrations. MeSH closely tracked DMS throughout ($R^2 = 0.56$), indicative of their shared DMSP source. However, MeSH concentrations were roughly a factor of five lower, averaging 16 ± 13 ppt. Both DMS and MeSH were highest in the early mornings hours when their oxidative loss was at a minimum and lowest in the afternoons. The average and interquartile range of the nighttime concentration ratio (Hr. 0-7) of $[\text{DMS}]/[\text{MeSH}]$ was 6.5 (4.3-7.5) (Fig. 2). This is in line with existing measurements of the emission flux ratio of $E_{\text{DMS}}/E_{\text{MeSH}}$ in coastal Southern California (5.5 ± 3.0) (Novak et al., 2022) and in the Southwest Pacific (3-7) (Lawson et al., 2020), and concentration ratio measurements of $[\text{DMS}]/[\text{MeSH}]$ in a low oxidant mesocosm experiment during typical coastal ocean biological conditions (4.60 ± 0.93) (Kilgour et al., 2022).

HPMTF measured significantly lower in concentration than its precursor DMS, with a 24-hour average of 0.7 ± 1.1 ppt and afternoon average (Hr. 13-17) of 1.6 ± 1.7 ppt. The median and interquartile ranges of $[\text{DMS}]/[\text{HPMTF}]$ across all data points were 317 (73-1797). HPMTF also exhibited a strong diurnal profile, peaking in the late afternoons between the hours of 13 and 17 and was mostly at or below the detection limit in the nights and early mornings. Its near-zero concentrations in the early mornings suggested that HPMTF production from DMS restarted daily. The afternoon maximum in HPMTF and minimum in DMS resulted in low and stable $[\text{DMS}]/[\text{HPMTF}]$ ratios during the afternoons, which are exploited in the box model analysis in Section 3.2.2.



260 **Figure 1: Hourly averaged time series of (a) DMS measured by RT-Vocus and wind speed, (b) MeSH measured by RT-Vocus, (c) HPMTF measured by Vocus AIM with iodide reagent ions, and (d) site-measured 3D cloud fraction (CF_{3A}) calculated according to Eq. 3.**

265 CF_{3A} during the study averaged 0.28 ± 0.27 , where the standard deviation reflects natural variability in cloud cover. Numerous time points of CF_{3A} were near 1, indicating full cloud filling the region horizontally and vertically within the boundary layer. Maximum daily CF_{3A} occurred in the morning and steadily declined throughout the day into the evening. The sky imager used to measure CF_H only collected data during daylight, resulting in no nighttime information on CF_{3A} at this site. The sky imager cloud mask retrieval was also optimized for later in the day, which could lead to false or exaggerated clouds in the dusk and dawn and might have influenced the peak CF_{3A} in the mornings. During the entire study, $[DMS]/[HPMTF]$ exhibited a weak positive correlation with CF_{3A} ($R^2 = 0.27$) (Fig. S3).

270

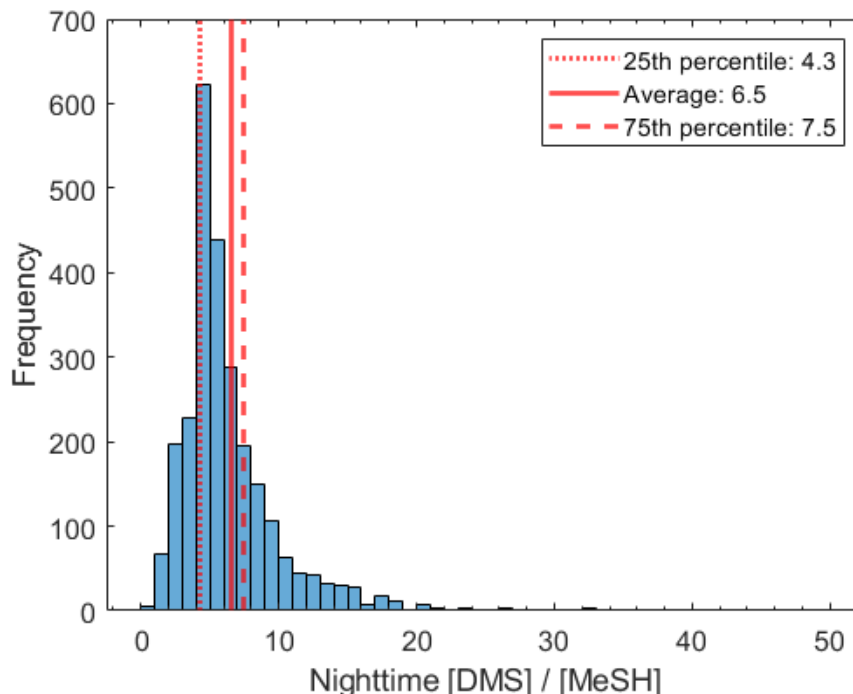


Figure 2: Histogram of five-minute averaged [DMS]/[MeSH] ratio during Hr. 0-7 when oxidative loss was at a minimum.

275 3.2 Measurement-constrained box model to assess cloud loss rates

3.2.1 Sensitivity to meteorological and chemical constraints

The model was run with a constant temperature diurnal profile corresponding to the diurnally-averaged measurements during the study, averaging 292 K. At this temperature, 61% of DMS OH-oxidation occurred by H-abstraction, which could later form HPMTF, and 39% occurred by OH-addition with no potential formation of HPMTF (Fig. S4). The diurnal-average temperature-dependent MTMP isomerization rate forming HPMTF was 0.036 s^{-1} (Assaf et al., 2023). The ambient temperature in this study was lower than for which this rate constant was experimentally measured (314-433 K) and is calculated based on the extrapolation in Assaf et al. (2023). Model NO, HO₂, and RO₂ concentrations at Hour 15 were 2, 12, and 36 ppt, respectively, resulting in an α_{HPMTF} , defined previously as the yield of HPMTF from the DMS H-abstraction pathway, of 0.85. Running the model with a time-varying temperature corresponding to the observed range over six weeks in the study (minimum 285 288 K - maximum 296 K) would result in a 31% increase in the diurnally-averaged HPMTF production rate and 9% decrease in afternoon [DMS]/[HPMTF].



290 Additionally, at a boundary layer height of 1000 m and exchange velocity of 0.5 cm s^{-1} between the boundary layer and free troposphere, 74% of DMS in the model was oxidized in the boundary layer and 26% was oxidized in the free troposphere above. The fraction of DMS oxidized in the boundary layer is highly dependent on the boundary layer height and exchange velocity (Fig. S5), both of which have considerable uncertainty in the marine atmosphere, where boundary layers can be stable, without a strong inversion layer, and mixing between the free troposphere is difficult to measure (Faloona, 2009). The following analysis and discussion represent DMS oxidation in the Azores-region MBL. The lower temperature in the free troposphere would shift DMS OH-oxidation toward OH-addition and slow down the MTMP isomerization rate forming HPMTF (Assaf et al., 2023). At a representative summertime free troposphere temperature in this region of 283 K, the percentage of DMS OH-oxidation occurring by H-abstraction would reduce to 46% and the MTMP isomerization rate would slow to 0.016 s^{-1} ; both reductions indicate the production of DMS-derived SO_2 and OCS would be lower in the free troposphere than in the MBL.

3.2.2 Evaluation of HPMTF loss rates

300 Figure 3a shows modelled $[\text{DMS}]/[\text{HPMTF}]$ for several cloud loss rates. Cloud loss was modelled as a constant first order sink with respect to HPMTF concentration. In the modelled clear sky, where HPMTF was only lost by gas-phase oxidation, aerosol uptake, and deposition, $[\text{DMS}]/[\text{HPMTF}]$ ranged between 4.2 and 12.7 during the course of a day. $[\text{DMS}]/[\text{HPMTF}]$ in the afternoon, between hours 13 and 17, averaged 4.5 ± 0.5 in the modelled clear sky. This afternoon range corresponded to the diurnal maximum in HPMTF concentration and diurnal minimum in $[\text{DMS}]/[\text{HPMTF}]$. Since HPMTF was often at or below the detection limit in the nighttime, Hr. 13-17 are used to interpret model-measurement comparison. Furthermore, the near-zero nighttime HPMTF concentrations throughout the study meant HPMTF production restarted daily with OH production, suggesting only cloud cover along the air mass back trajectory in the hours between sunrise and the end of the model-measurement comparison period (Hr. 17) impacted HPMTF chemistry in the model. Since no consistently clear sky day existed during the study, a close case, occurring on July 11, was used to assess how well the model captured HPMTF chemistry in low cloud fraction conditions. Average CF_{3A} on July 11 between Hr. 6 and 17 was 0.065 ± 0.055 (Fig. 3b, Fig. 3c), and the average afternoon $[\text{DMS}]/[\text{HPMTF}]$ was 7.6 ± 1.1 . This is slightly above the clear sky $[\text{DMS}]/[\text{HPMTF}]$ (Fig. 3a), which could be due to a small amount of cloud cover overhead, cloud presence along the trajectory prior to the afternoon $[\text{DMS}]/[\text{HPMTF}]$ comparison period, and/or uncertainty in the non-cloud HPMTF loss rates. Nonetheless, the close agreement indicates that DMS-HPMTF chemistry in the model is reasonably well-captured for the clear sky case and highlights that a large HPMTF loss to photolysis is not necessary, as has been implied previously (Khan et al., 2021).

The HPMTF cloud loss term was determined for all study days. The rate of cloud loss was determined as the value needed to make up the residual difference between the modelled clear sky $[\text{DMS}]/[\text{HPMTF}]$ in the afternoon and the measurements of afternoon $[\text{DMS}]/[\text{HPMTF}]$. For example, to match the observed $[\text{DMS}]/[\text{HPMTF}]$ on July 11, a small cloud loss term of 0.24 h^{-1} was required. This is also shown for two additional days in Fig. 3, July 3 and June 27. For July 3, a cloud loss term of 0.94



h^{-1} was needed for the model to match the measured afternoon $[\text{DMS}]/[\text{HPMTF}]$ of 20 ± 3 . For June 27, a cloud loss term of 2.5 h^{-1} was needed for the model to match the measured afternoon $[\text{DMS}]/[\text{HPMTF}]$ of 49 ± 12 . As expected, days with the faster cloud loss rates have higher $\text{CF}_{3\text{A}}$, where the $\text{CF}_{3\text{A}}$ between Hr. 6 and Hr. 17 was 0.17 ± 0.10 for July 3 and 0.29 ± 0.22 for June 27.

325

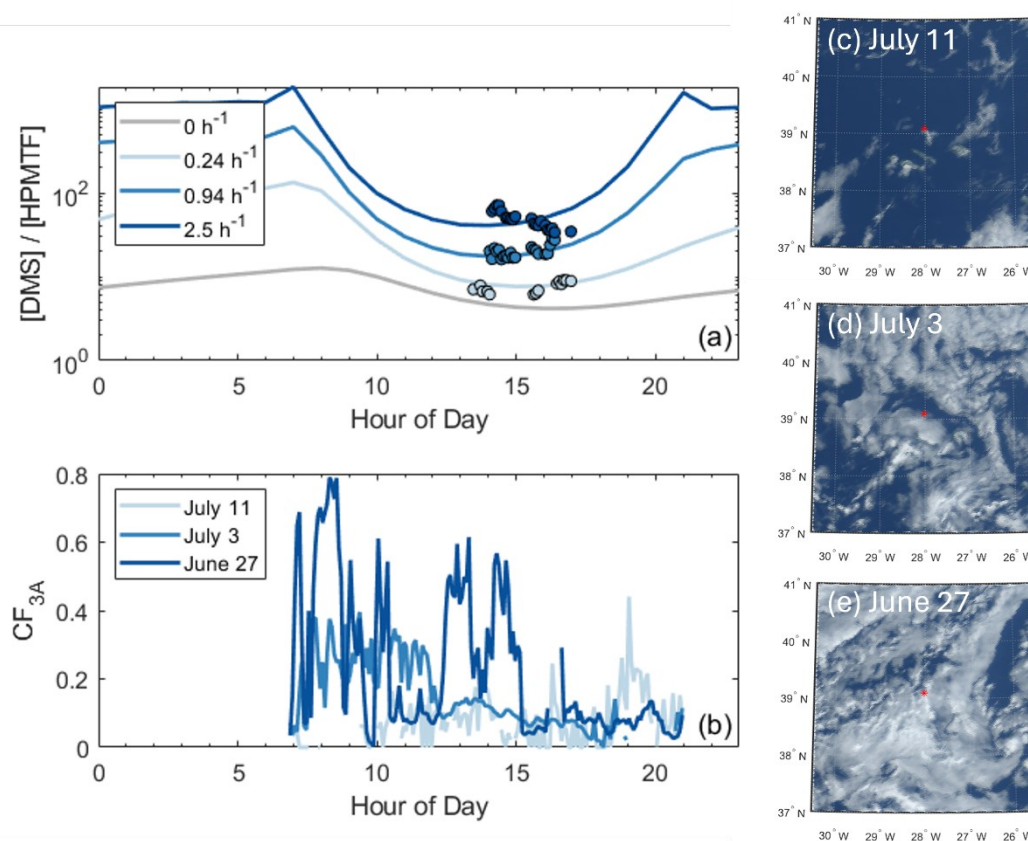
The days shown in Fig. 3 were selected as case studies as they displayed a range in $\text{CF}_{3\text{A}}$ and had unstable, well-mixed boundary layers based on vertical profiles in potential temperature and water vapor mixing ratio (Fig. S6). Unstable, well-mixed boundary layers occurred on 16 of the 31 study days. During these conditions, we expect that the ground-based measurements of $[\text{DMS}]/[\text{HPMTF}]$ are similar to $[\text{DMS}]/[\text{HPMTF}]$ throughout the boundary layer due to strong vertical mixing. As a result, the inferred cloud loss terms from $[\text{DMS}]/[\text{HPMTF}]$ for these days is interpreted as an estimate of the cloud entrainment rate, thought of as the mixing rate of clear air into cloud. The three days in Fig. 3 were also chosen because they had more uniform cloud fraction during the time of HPMTF production. In an ideal case, where cloud fraction and cloud type are constant, measured $[\text{DMS}]/[\text{HPMTF}]$ would fall exactly along the modelled $[\text{DMS}]/[\text{HPMTF}]$. In practice, $\text{CF}_{3\text{A}}$ varies throughout the day (Fig. 3b) due to changes in boundary layer height and horizontal cloud cover, and the GOES images (NOAA National Centers for Environmental Information, 2017) in Fig. 3cde represent only one snapshot in time. It is more likely that the HPMTF cloud loss term changes throughout the day as $\text{CF}_{3\text{A}}$ in the sampling region evolves. As a result, extending this method to all study days incorporates some uncertainty in the derived cloud loss terms due to the cloud field at the site changing during the time period of HPMTF production.

340 Following the approach outlined above, we derive cloud loss rates based on the residual loss required for modelled $[\text{DMS}]/[\text{HPMTF}]$ to equal the measured $[\text{DMS}]/[\text{HPMTF}]$ ratio for all 31 days. This approach enables cloud loss terms to be derived over long time periods and significantly increases the data coverage compared to prior work. However, the indirect methodology of assigning cloud loss terms based on residual differences in $[\text{DMS}]/[\text{HPMTF}]$ from a base case means any inaccuracy in the model (e.g. rates of other HPMTF loss processes, variable fractions of DMS forming HPMTF based on changing temperature and NO and RO_2 concentrations) can contribute to uncertainty in the derived cloud loss terms. Additionally, we are utilizing near-surface measurements of $[\text{DMS}]$ and $[\text{HPMTF}]$, which is less ideal compared to making vertically-resolved measurements of these species, or direct airborne eddy covariance flux measurements at different altitudes to directly calculate HPMTF loss terms (Novak et al., 2021). Figure 4 displays the loss rates of HPMTF to cloud, aerosol, dry deposition, and OH for each day following this approach. Aerosol uptake and dry deposition accounted for a minor fraction of HPMTF loss during this study, while gas-phase oxidation by OH and loss to cloud made more significant contributions. Bracketing the modelled outputs based on the uncertainty in cloud loss rates derived from $[\text{HPMTF}]$ uncertainty, on average, 79-91% of HPMTF in the model was lost to cloud, 7-16% was lost to OH, and the remaining 2-6% was lost to aerosol and dry deposition. The reported loss of HPMTF to aerosol is likely a lower limit as any acidity in the ambient marine aerosol (Angle et al., 2021) could cause enhanced HPMTF uptake (Liggio and Li, 2006). Additionally, we do not have concurrent

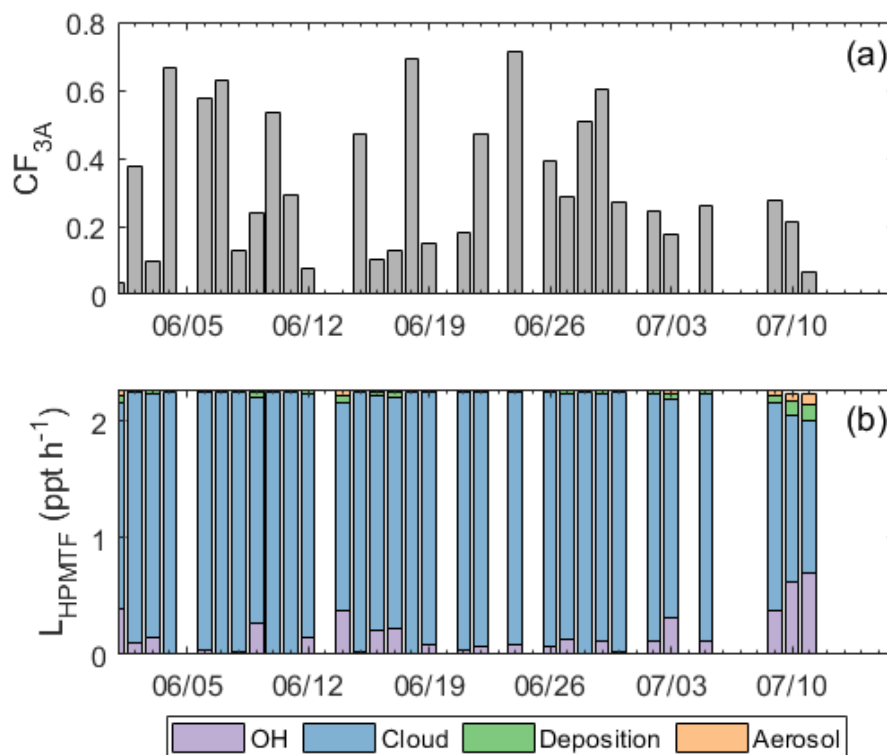
350



355 measurements of coarse mode ($> 1 \mu\text{m}$ diameter) sea spray aerosol particles which are hygroscopic (Zieger et al., 2017) and could provide an enhanced surface area for HPMTF uptake, particularly during strong winds that promote sea spray production. However, this loss process is still expected to be small relative to cloud due to the large difference in surface area between aerosol and cloud droplets. HPMTF was lost to cloud chemistry at a rate approximately 5-13 times faster than to OH chemistry during this study. Regardless of the uncertainty in cloud loss rates, this analysis highlights that cloud loss is the dominant
 360 HPMTF loss process in the MBL during this study. The median lifetime of HPMTF to cloud bracketed by uncertainties in HPMTF quantification were 0.29-0.81 h (interquartile range of 0.06-2.24 h), which were significantly faster than the instantaneous chemical lifetime to OH (greater than 4 h). This is consistent with airborne measurements in Novak et al. (2021) off the coast of Southern California, where the lifetime of HPMTF to cloud (1.2 ± 0.6 h) was also much faster than the lifetime to OH (greater than 5 h). Analysis in this work affirms cloud chemistry as the dominant HPMTF loss pathway now over a
 365 longer time period and in another region of the MBL.



370 **Figure 3: (a) Modelled [DMS]/[HPMTF] for different HPMTF cloud loss rates, using the formic acid calibration factor for HPMTF, which represents upper limits on cloud loss rates. The gray line with a cloud loss term of 0 h^{-1} represents the modelled clear sky. Scattered points represent 5-minute averaged [DMS]/[HPMTF] measurements for colors matching the dates in (b). (b) Site-measured 3-dimensional cloud fraction (CF_{3A}) for three selected days during the study. GOES imagery for $4^\circ \times 5^\circ$ regions around Graciosa Island at Hour 15 for (c) July 11, (d) July 3, and (e) June 27. The approximate measurement location on Graciosa Island (39.0916° N , 28.0257° W) is marked with a red asterisk.**



375 **Figure 4: (a) Site-measured 3-dimensional cloud fraction (CF_{3A}) for days with modelled HPMTF loss rates. (b) Histogram of modelled HPMTF loss rates for the 31 study days, separated by HPMTF loss to OH, cloud, deposition, and aerosol. Breakdown of HPMTF loss rates corresponds to the model run with a formic acid calibration factor for HPMTF, resulting in an upper limit on the fraction of HPMTF lost to cloud.**

4 Discussion

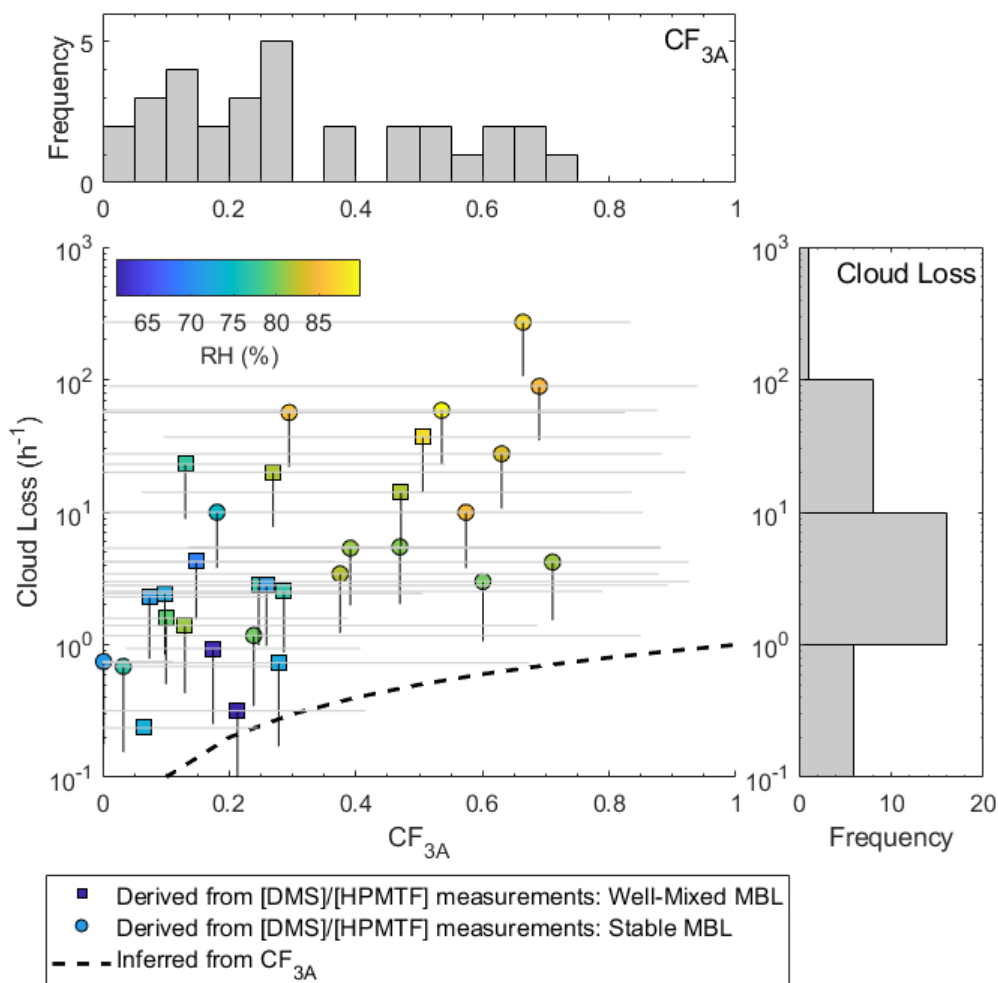
4.1 Dependence of cloud loss rates on site-measured 3-dimensional cloud fraction

380 The HPMTF cloud loss rates inferred from the model-measurement comparison of $[DMS]/[HPMTF]$ for all 31 study days are scattered against CF_{3A} in Fig. 5 and colored by afternoon relative humidity. Higher cloud loss rates of HPMTF were observed on days with increased relative humidity, indicative of sampling in a cloud-filled boundary layer (Chernykh and Eskridge, 1996). Additionally, since the relative humidity across all days, even at low CF_{3A} , was above the efflorescence point of inorganic sea spray aerosol (50%) (Zieger et al., 2017), we expect the variability in inlet loss (assuming the inlet is coated in wet sea spray aerosol) was minimal and take the observed trend to be robust. Across all days, the median cloud loss rate of HPMTF to cloud, bracketed by uncertainties in HPMTF quantifications, was $1.2\text{-}3.4 \text{ h}^{-1}$ (interquartile range $0.45\text{-}19 \text{ h}^{-1}$). In just the days with unstable, well-mixed boundary layers demarcated with squares in Fig. 5, the median and interquartile ranges of cloud loss rates were $0.86\text{-}2.5 \text{ h}^{-1}$ and $0.34\text{-}9.2 \text{ h}^{-1}$, respectively. Inferring HPMTF cloud loss rates from ground-based

385



390 measurements of [DMS]/[HPMTF] relies on the assumption that the near-surface [DMS]/[HPMTF] measurements are
representative of [DMS]/[HPMTF] throughout the boundary layer. While this is a fair assumption in well-mixed boundary
layers with strong vertical mixing, this is likely not the case in stable boundary layers. In well-mixed boundary layers, the rate
of HPMTF cloud loss can be thought of as the entrainment of HPMTF in clear air into cloud, which has previously been
estimated at 1 h^{-1} for stratocumulus clouds based on large eddy simulation studies (Feingold et al., 1998). Our derived cloud
loss rates on the well-mixed days are closer to these values. The dashed black line in Fig. 5 shows the predicted cloud loss of
395 HPMTF based on an average 1 h^{-1} entrainment rate. While our HPMTF cloud loss rates are faster than those predicted, they
follow the same shape where cloud loss increased and saturated with increasing CF_{3A} . Unlike the prediction, the derived
HPMTF cloud loss rates were variable for individual CF_{3A} . This is likely a result of heterogeneity in cloud fraction (Fig. 3b)
and cloud type during the time period of HPMTF production, which are ignored in the calculation of the predicted rate. One
particularly important aspect of cloud heterogeneity affecting the calculations can come in instances of near-complete vertical
400 cloud fraction, as HPMTF was likely lost to cloud at the diffusion limit, which is not well-captured by the inferred cloud loss
from CF_{3A} alone and can result in fast cloud loss rates.



405 **Figure 5: Relationship between derived cloud loss rates and CF_{3A} measured at the site. Scattered data points represent derived cloud loss terms based on the residual in $[DMS]/[HPMTF]$, where HPMTF was calibrated with the formic acid calibration factor, and are colored by afternoon relative humidity in Hr. 13-17. Square points represent days with a well-mixed MBL, defined by near-vertical slopes in potential temperature and water mixing ratio, and circles represent a stable, not well-mixed MBL, defined by non-zero slopes in potential temperature and water mixing ratio. Black vertical lines below the points represent the range in cloud loss rates based on HPMTF uncertainty. Gray horizontal lines across the points represent the minimum and maximum CF_{3A} during the time of HPMTF production from Hr. 6-410 17. The black dotted line represents an expected cloud loss term calculated as the product of CF_{3A} and an assumed 1 h^{-1} entrainment rate. The variability in CF_{3A} and cloud loss are also shown as histograms on the mirrored axes.**

4.2 Impacts of cloud loss on MBL DMS conversion to SO_2 and OCS

The efficient removal of the HPMTF intermediate via cloud chemistry has a correspondingly large impact on the amount of SO_2 and OCS derived from DMS oxidized in the MBL. Figure 6 shows the fraction of DMS converted to SO_2 and OCS in the



415 modelled clear sky case (black dashed line) and when implementing the derived cloud loss rates from [DMS]/[HPMTF] (blue
histogram). In both cases, the converted fraction is calculated as the 24-hour average of the production rate of the product from
DMS divided by the chemical loss rate of DMS. In clear sky conditions, 27% of DMS oxidized in the MBL is converted to
SO₂ (Fig. 6a) and 3% of DMS oxidized in the MBL is converted to OCS (Fig. 6b). This analysis indicates that HPMTF cloud
loss, at rates derived from [DMS]/[HPMTF], could decrease MBL DMS-derived SO₂ by on average 52-60% (Fig. 6a) and
420 MBL DMS-derived OCS by on average 80-92% (Fig. 6b), where the ranges correspond to uncertainty in cloud loss terms
derived from HPMTF quantification uncertainty. These findings are consistent with earlier, global modeling work based on
an HPMTF cloud loss rate determined from a flight off the coast of Southern California (Novak et al., 2021) that showed
HPMTF cloud loss reduced global DMS-derived SO₂ production by 35% (Novak et al., 2021) and OCS production by 92%
(Jernigan et al., 2022a).

425

The oxidation of SO₂ to sulfuric acid has been shown to result in new particle formation in the MBL (Covert et al., 1992).
Reduction in MBL SO₂ due to cloud chemistry shown here suggests that nucleation and growth rates of new particles in the
MBL might be slower than previously thought, or non-SO₂ precursors, such as ammonia (Jokinen et al., 2018) and iodine-
containing molecules (Baccarini et al., 2020) might play larger roles than once believed, especially in cloudy regions.
430 Importantly, aqueous phase HPMTF chemistry in cloud has been shown to promptly form SO₄²⁻ at unit yield (Jernigan et al.,
2024). Including prompt sulfate production from HPMTF cloud chemistry in our model leads to the production of 0.18-0.20
μg m⁻³ SO₄²⁻ daily for the median derived cloud loss rate of 1.2-3.4 h⁻¹. This means that although HPMTF cloud chemistry
largely reduces SO₂ concentrations in the MBL, sulfate aerosol is still being formed in cloudy regions, albeit through a different
mechanism. Additionally, the DMS oxidation products along the OH-addition pathway (DMSO, DMSO₂, MSIA, and MSA)
435 are also soluble. If they are irreversibly lost to cloud like HPMTF, then cloud chemistry could even more drastically control
the production of DMS-derived products. Lastly, by decreasing the amount of OCS produced from DMS in the MBL, HPMTF
cloud loss reduces the amount of OCS that is transported to the stratosphere (Montzka et al., 2007), where it can serve as a
precursor to stratospheric SO₄²⁻ and control Earth's radiative budget (Brühl et al., 2012; Kremser et al., 2016).

440 **4.3 Comparison between DMS oxidation using derived cloud loss rates and current implementations of DMS oxidation in global models**

The conversion of MBL DMS to SO₂ and OCS incorporating cloud loss rates derived from *in situ* measurements of
[DMS]/[HPMTF] are compared to the conversions of DMS to SO₂ and OCS from DMS oxidation in common global model
implementations. Without incorporating HPMTF chemistry, the global chemical transport model, GEOS-Chem, assigns direct,
fixed yields of SO₂ (1, 1, 0.75) and MSA (0, 0, 0.25) from NO₃-oxidation, OH-oxidation H-abstraction, and OH-oxidation
445 OH-addition pathways, respectively (Chin et al., 1996). At the limit of no cloud present, this yield implementation results in
93% of MBL DMS converted to SO₂ in the F0AM box model, which is significantly larger than the amount of SO₂ formed
when implementing the [DMS]/[HPMTF] derived cloud loss rates. The historical model of OCS formation from DMS OH-



oxidation also uses a direct, fixed yield of 0.007 (Barnes et al., 1994), which aligns with our findings here in the presence of cloud.

450

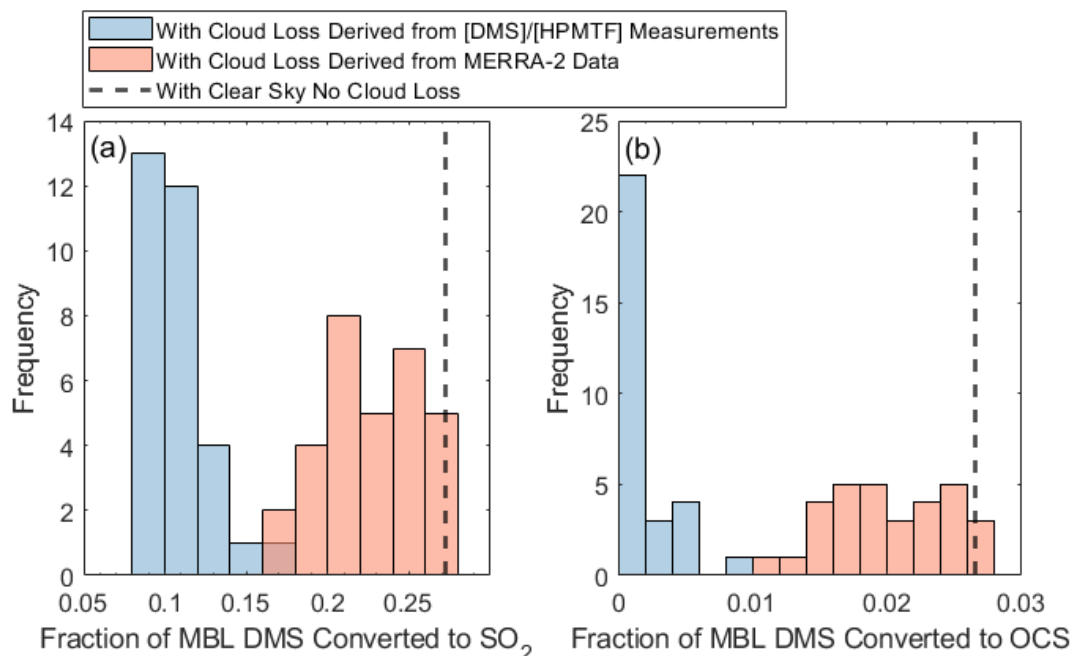
As introduced earlier, when taking into account cloud chemistry, GEOS-Chem parameterizes cloud loss of reactive, soluble gases as the product of the boundary layer grid cell MERRA-2 cloud fraction (CF_{3M}) (Global Modeling and Assimilation Office (GMAO), 2015) (Holmes et al., 2019) and an average entrainment rate of 1 h^{-1} based on large eddy simulation studies of stratocumulus clouds (Feingold et al., 1998). This cloud loss term that would be input into GEOS-Chem was run in the developed F0AM box model, with HPMTF chemistry, to assess how closely it matched the modelled outputs from the derived cloud loss terms; the results of this analysis are shown by orange bars in Fig. 6. Utilizing a cloud loss rate for HPMTF determined by CF_{3M} resulted in on average, a factor of 1.7-2.1 and 3.7-9.5 more MBL DMS-derived SO_2 and OCS, respectively, compared to the derived $[\text{DMS}]/[\text{HPMTF}]$ cloud loss rate implementation, where the ranges indicate propagated uncertainty from HPMTF concentrations. These MERRA-2-based values were closer to the fractions of SO_2 and OCS formed from DMS in the modelled clear sky case. This is partly due to the consistent underestimate by up to a factor of four of CF_{3M} relative to CF_{3A} during June and July (Fig. 7). This is consistent with significant errors in the accuracy of satellite-derived cloud fractions in the MBL where the boundary layer is low and where there is persistent cloud cover (Kuma et al., 2020). Our analysis using *in situ* derived cloud loss rates and site measurements of 3D cloud fraction suggest that (1) cloud processing in models is required to accurately capture the fate of DMS, and (2) cloud loss parameterized by satellite-retrievals of low-level

455

460



465 cloud fraction underestimate the effects of HPMTF cloud chemistry. Models might better capture the impacts of HPMTF cloud chemistry by assuming full conversion to SO_4^{2-} when cloud is present and conversion to SO_2 in clear sky conditions.



470 **Figure 6: Fraction of MBL DMS converted to (a) SO_2 and (b) OCS shown for the derived cloud loss rates based on residual $[\text{DMS}]/[\text{HPMTF}]$ and based on the MERRA-2 cloud fractions and a 1 h^{-1} entrainment rate. The modelled clear sky conversion, using HPMTF chemistry and heterogeneous loss of DMS oxidation products, is in black.**

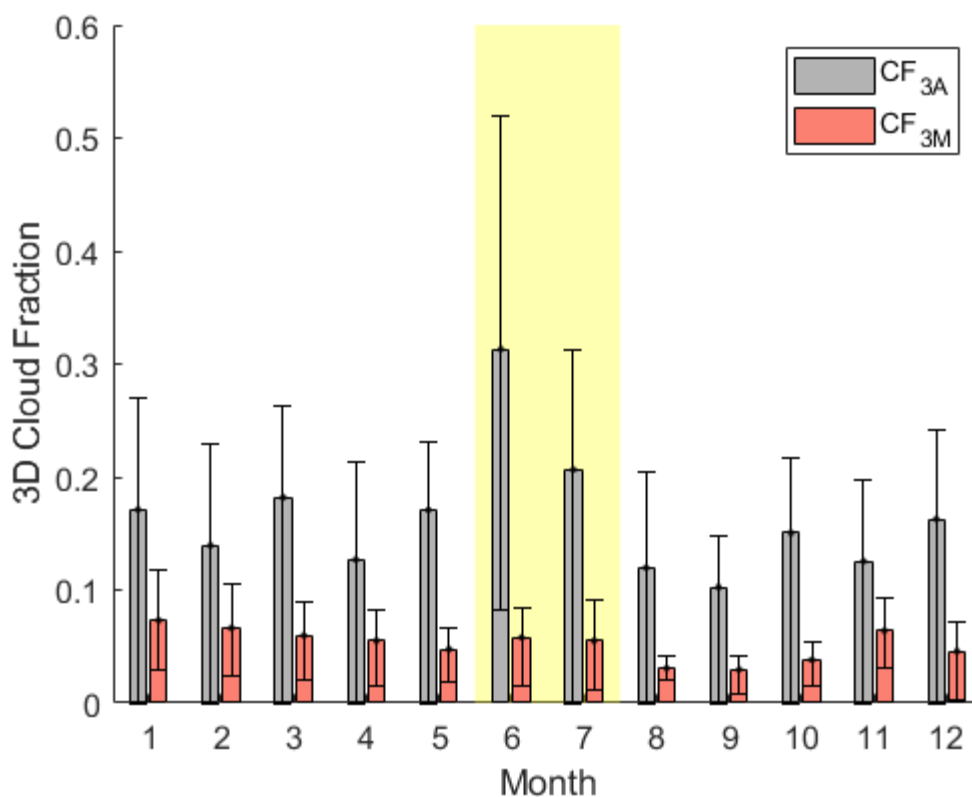
4.4 Insights into DMS-oxidation year-round

In situ DMS, HPMTF, and CF_3A measurements show fast cloud processing strongly regulates the fate of HPMTF, to a greater extent than what's currently prescribed in global models, during the study in June and July of 2022. Using DMS climatology and year-round measurements made at ENA, we build upon the summertime chemical box model to speculate on the role of cloud processing in DMS-oxidation in this region during time periods beyond the summer intensive period. Monthly-averaged DMS fluxes were taken from Hulswar et al. (2022) climatology for an 8° radius box around Graciosa, approximating the DMS lifetime. Monthly OH profiles were determined in F0AM using the hybrid method for calculating photolysis frequencies with default surface albedo and O_3 column (Wolfe et al., 2016), and validated by the OH climatology in Spivakovsky et al. (2000). Monthly-averaged site measurements of meteorological (pressure, temperature, and relative humidity) (Uin et al., 2019) and boundary layer height data (Heffter, 1980) were used as inputs. Remaining trace gas constraints, dilution terms, and non-cloud HPMTF loss processes were kept constant from the summertime model.

In the model, we demonstrate that the clear sky HPMTF concentration in fall and winter months is reduced relative to its concentration in spring and summer months, in line with our understanding of its production as a function of DMS and oxidant



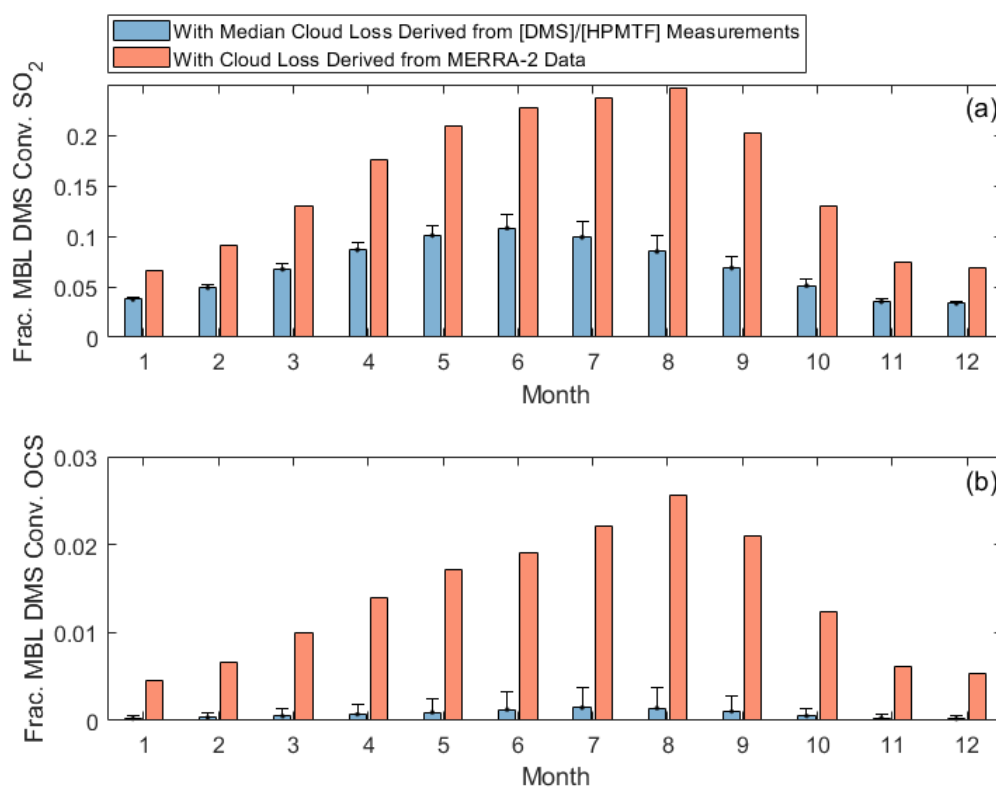
485 concentration, temperature, and boundary layer height. Dissolved DMS concentrations are highest in this region during the
 spring and summer months (<6 nM), and are low in other months (<2 nM) (Hulswar et al., 2022). Similarly, air temperature
 in the MBL is lower in months outside of this study period, with sonde profiles at ENA indicating a wintertime MBL
 temperature of 10 °C is representative. At this temperature, only 46% of DMS OH-oxidation occurs by H-abstraction
 (compared to 61% in the summertime model), and the MTMP isomerization rate is approximately halved. Lower daylight
 490 hours in non-summer months reduce OH concentrations; global OH climatology indicates surface OH at this latitude is close
 to a factor of 10 lower in January compared to July (Spivakovsky et al., 2000). Furthermore, modelled NO and RO₂
 concentrations are roughly a factor of two higher in July than in January, though still low, resulting in α_{HPMTF} of 0.86 in July
 and α_{HPMTF} of 0.89 at Hour 15 in January. BLHs are less sensitive to seasonality at this site, with average wintertime BLHs
 roughly 20% higher than typical heights observed during June and July. The low precursor DMS concentration, increased
 495 preference for the DMS OH-addition channel, slower MTMP isomerization rate, and reduced oxidative conditions result in
 modelled HPMTF production being approximately six times slower in January compared to July.



500 **Figure 7: Monthly mean boundary layer 3D cloud fraction measured at the site by ARM in gray (CF_{3A}) and measured by MERRA-2 (CF_{3M}) surrounding Graciosa in red. Error bars represent the interquartile ranges. Both CF_{3A} and CF_{3M} are calculated based on the boundary layer height determined by the Heffter approximation. The yellow shaded region indicates the time period of this study.**



While HPMTF production is lower beyond June and July of this study, measurements of CF_{3A} demonstrate 3D cloud fraction at ENA is large year-round, shown in Fig. 7. CF_{3A} peaks in June during this study, but other months in the year are consistent with CF_{3A} observed in July, during which some of our DMS and HPMTF measurements were made. Applying the median cloud loss rates derived from summertime $[DMS]/[HPMTF]$ ($1.2\text{-}3.4\text{ h}^{-1}$) to all months, we demonstrate a low fraction of DMS ultimately forms SO_2 (3-12%) and OCS ($<0.4\%$) at this site year-round (Fig. 8). Furthermore, applying a monthly-specific cloud loss rate derived from average CF_{3M} from MERRA-2 and a 1 h^{-1} entrainment rate indicates MERRA-2 continues to overestimate the amount of SO_2 and OCS produced from DMS across the entire year (Fig. 8). Together, these findings indicate that cloud processing plays a large role in DMS-oxidation in the ENA MBL year-round, and persistent underestimates in 3D cloud fraction by MERRA-2 likely result in current global models underrepresenting the dominant impact of cloud chemistry across the entire year.



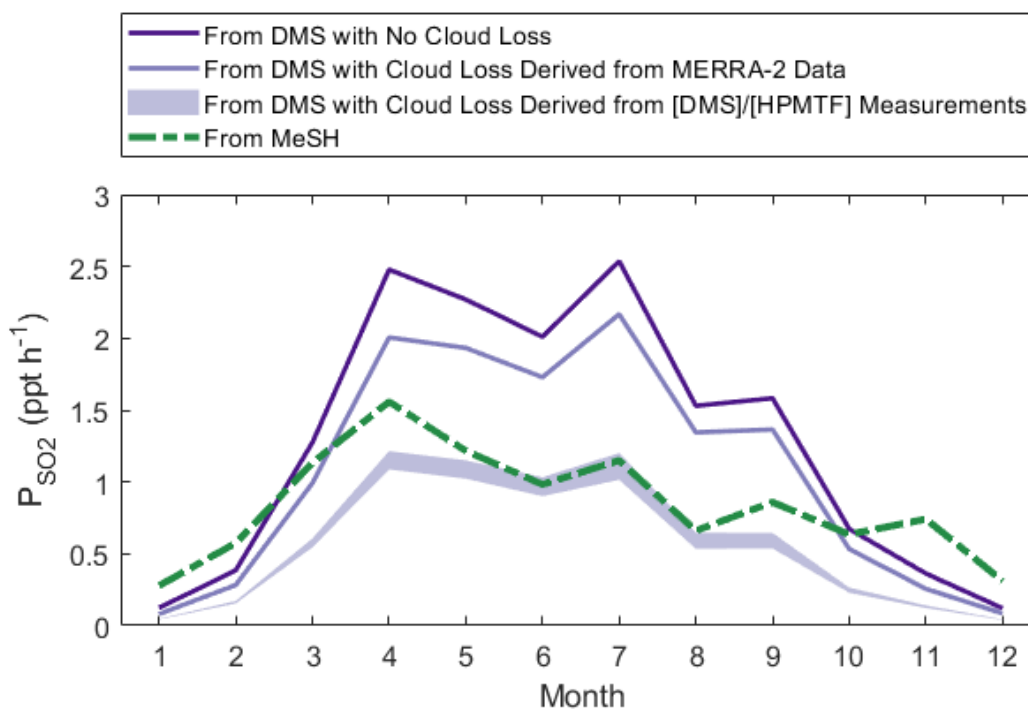
515 **Figure 8: Diurnally-averaged fractions of MBL DMS converted to (a) SO_2 and (b) OCS in the year-round model. Derived cloud loss bars indicate running the model with the upper limit of the median cloud loss range ($1.2\text{-}3.4\text{ h}^{-1}$) and the error bar represents running the model with the lower limit of the range applied to all months. MERRA-2 cloud loss bars indicate running the model with monthly-specific cloud loss rates calculated as the product of the monthly averaged CF_{3M} and a 1 h^{-1} entrainment rate.**



520 Finally, we contextualize the impact of cloud processing on SO₂ production through a model test including MeSH. Assuming the loss rate of HPMTF to cloud derived in this study (1.2-3.4 h⁻¹ median) is representative of its loss rate in other seasons, then cloud chemistry can reduce the production of SO₂ from DMS by 49-67% year-round compared to the clear sky case, shown in Fig. 9. Given MeSH is an efficient MBL SO₂ source with a short lifetime to OH and its oxidation toward SO₂ does not proceed via the soluble HPMTF intermediate, it has the potential to further close the SO₂ budget. Utilizing a flux of MeSH at 20% of the monthly-averaged DMS flux for this region (Hulswar et al., 2022), in line with the limited current measurements of flux ratios of DMS and MeSH (Lawson et al., 2020; Novak et al., 2022), shows MeSH (green in Fig. 9) can be competitive with DMS (purple in Fig. 9) as an SO₂ source in this region, where its oxidation has minimal temperature-dependence (Chen et al., 2023). MeSH is an especially important SO₂ source when accounting for cloud processing of HPMTF at the derived cloud loss rates, and in winter months, when preference for DMS OH-addition and slow MTMP isomerization limit SO₂ yielded from DMS-oxidation.

525

530



535 **Figure 9: Diurnally-averaged SO₂ production rates determined by the year-round model, where contributions to SO₂ from MeSH (green) and DMS (purple) are run individually. SO₂ production rates from DMS involving MERRA-2 cloud loss use monthly averaged CF_{3M} and a 1 h⁻¹ entrainment rate, and production rates from DMS involving the derived cloud loss rates from [DMS]/[HPMTF] use the median cloud loss rates (1.2-3.4 h⁻¹) applied to all months.**



5 Conclusions

This work utilizes measurements of the reactant and product pair, DMS and HPMTF, and a developed box model constrained by meteorological and trace gas measurements at the site to derive the loss rate of HPMTF to cloud in the ENA MBL during June and July 2022. This method was enabled by the considerable source of DMS from the oceans, and its large reservoir in the soluble oxidation product, HPMTF. The median derived cloud loss rate based on [DMS]/[HPMTF] analysis was 1.2-3.4 h⁻¹, leading to a median lifetime of HPMTF to cloud of 0.29-0.81 h. Box model analysis indicated cloud was the dominant sink of HPMTF, with on average, 79-91% of HPMTF lost to cloud, and 7-16% lost to the second strongest loss pathway, OH. Our findings are consistent with prior airborne flux analysis, where the HPMTF lifetime to cloud on a single flight leg was similarly fast (1.2 ± 0.6 h) and similarly outpaced chemistry.

545

Our study demonstrates that cloud loss scaled with site-measured 3D cloud fraction over six weeks and controlled the fate of HPMTF in the MBL throughout this entire period. The chemically-derived cloud loss rates resulted in modelled reductions in DMS-derived MBL SO₂ and OCS of 52-60% and 80-92%, respectively. Since cloud processing sets MBL SO₂ and SO₄²⁻ aerosol budgets from DMS, additional, highly sensitive measurements of MBL SO₂, DMS, and the other major marine SO₂ precursor, MeSH, are warranted to constrain drivers of SO₂ and new particle formation through the production of H₂SO₄. Lastly, this work utilizes DMS climatology and year-round measurements at ENA to suggest that cloud processing of HPMTF is important year-round in the ENA, beyond the measurement period, due to persistent boundary layer cloud cover. Since satellite products, like MERRA-2, retrieve low cloud fractions relative to *in situ* ground-based measurements, and global chemical transport models parameterize cloud loss by satellite cloud fraction, the controlling role of cloud processing in setting SO₂, OCS, and SO₄²⁻ budgets is likely underrepresented in current global models.

555

Data availability

DMS, MeSH, and HPMTF time series are available at <http://digital.library.wisc.edu/1793/85493> (Kilgour and Bertram, 2024)

Supplement

Contains details on the HPMTF measurement and uncertainty, supporting figures, and box model constraints.

560 Author contributions

DBK, CMJ, and THB conceptualized the main ideas of the paper. DBK and CMJ collected RT-Vocus data, and processed and analyzed the data. SA and OG collected Vocus AIM data, with CM contributing to setup and supporting data analysis. OG analyzed Vocus AIM field data, and SA performed RH-dependent formic acid calibrations and analyzed calibration data. DBK



565 developed the box models and wrote the paper, with input from CMJ and THB. CM, MES, JW, JAT, PZ, and THB contributed to AGENA campaign planning and execution, and supported data collection and analysis. All authors reviewed and edited the paper.

Competing interests

At least one of the (co-)authors is a member of the editorial board of Atmospheric Chemistry and Physics.

Financial support

570 This material is based upon work supported by the U.S. Department of Energy, Office of Science, Office of Biological and Environmental Research, Atmospheric System Research (ASR) under Award Number DE-SC0021985. This research used resources of the Atmospheric Radiation Measurement (ARM) User Facility, which is a DOE Office of Science User Facility, under Award Number AFC010011.

Acknowledgments

575 The authors thank the ARM staff at ENA and Los Alamos National Laboratory, including Bruno Cunha and Tercio Silva, for their support and logistical contributions to the study, and the ARM instrument mentors, including Donna Flynn at Pacific Northwest National Laboratory, for providing publicly accessible supporting data from ENA. Additional thanks to Ankur Desai and Grant Petty at University of Wisconsin-Madison for valuable discussions on boundary layer stability. Lastly, the authors acknowledge Glenn Wolfe for providing the F0AM box model, some of which was edited for use in this analysis, and
580 the tofTools team for providing tools for mass spectrometry data analysis.

References

- Albrecht, B. A., Jensen, M. P., and Syrett, W. J.: Marine boundary layer structure and fractional cloudiness, *Journal of Geophysical Research: Atmospheres*, 100, 14209–14222, <https://doi.org/10.1029/95JD00827>, 1995.
- Alexander, B., Sherwen, T., Holmes, C. D., Fisher, J. A., Chen, Q., Evans, M. J., and Kasibhatla, P.: Global inorganic nitrate production mechanisms: comparison of a global model with nitrate isotope observations, *Atmospheric Chemistry and Physics*, 20, 3859–3877, <https://doi.org/10.5194/acp-20-3859-2020>, 2020.
- Andreae, M. O.: Ocean-atmosphere interactions in the global biogeochemical sulfur cycle, *Marine Chemistry*, 30, 1–29, [https://doi.org/10.1016/0304-4203\(90\)90059-L](https://doi.org/10.1016/0304-4203(90)90059-L), 1990.
- 590 Angle, K. J., Crocker, D. R., Simpson, R. M. C., Mayer, K. J., Garofalo, L. A., Moore, A. N., Mora Garcia, S. L., Or, V. W., Srinivasan, S., Farhan, M., Sauer, J. S., Lee, C., Pothier, M. A., Farmer, D. K., Martz, T. R., Bertram, T. H., Cappa, C. D.,



- Prather, K. A., and Grassian, V. H.: Acidity across the interface from the ocean surface to sea spray aerosol, *Proceedings of the National Academy of Sciences*, 118, e2018397118, <https://doi.org/10.1073/pnas.2018397118>, 2021.
- Antweiler, R. C. and Taylor, H. E.: Evaluation of Statistical Treatments of Left-Censored Environmental Data using Coincident Uncensored Data Sets: I. Summary Statistics, *Environ. Sci. Technol.*, 42, 3732–3738, <https://doi.org/10.1021/es071301c>, 2008.
- 595
- Assaf, E., Finewax, Z., Marshall, P., Veres, P. R., Neuman, J. A., and Burkholder, J. B.: Measurement of the Intramolecular Hydrogen-Shift Rate Coefficient for the CH₃SCH₂OO Radical between 314 and 433 K, *J. Phys. Chem. A*, 127, 2336–2350, <https://doi.org/10.1021/acs.jpca.2c09095>, 2023.
- Baccarini, A., Karlsson, L., Dommen, J., Duplessis, P., Vüllers, J., Brooks, I. M., Saiz-Lopez, A., Salter, M., Tjernström, M., Baltensperger, U., Zieger, P., and Schmale, J.: Frequent new particle formation over the high Arctic pack ice by enhanced iodine emissions, *Nat Commun*, 11, 4924, <https://doi.org/10.1038/s41467-020-18551-0>, 2020.
- 600
- Barnes, I., Becker, K. H., and Patroescu, I.: The tropospheric oxidation of dimethyl sulfide: A new source of carbonyl sulfide, *Geophysical Research Letters*, 21, 2389–2392, <https://doi.org/10.1029/94GL02499>, 1994.
- Barth, M. C., Ervens, B., Herrmann, H., Tilgner, A., McNeill, V. F., Tsui, W. G., Deguillaume, L., Chaumerliac, N., Carlton, A., and Lance, S. M.: Box Model Intercomparison of Cloud Chemistry, *Journal of Geophysical Research: Atmospheres*, 126, e2021JD035486, <https://doi.org/10.1029/2021JD035486>, 2021.
- 605
- Bates, T. S., Lamb, B. K., Guenther, A., Dignon, J., and Stoiber, R. E.: Sulfur emissions to the atmosphere from natural sources, *J Atmos Chem*, 14, 315–337, <https://doi.org/10.1007/BF00115242>, 1992.
- Berndt, T., Scholz, W., Mentler, B., Fischer, L., Hoffmann, E. H., Tilgner, A., Hyttinen, N., Prisle, N. L., Hansel, A., and Herrmann, H.: Fast Peroxy Radical Isomerization and OH Recycling in the Reaction of OH Radicals with Dimethyl Sulfide, *J. Phys. Chem. Lett.*, 10, 6478–6483, <https://doi.org/10.1021/acs.jpcelett.9b02567>, 2019.
- 610
- Bertram, T. H., Kimmel, J. R., Crisp, T. A., Ryder, O. S., Yatavelli, R. L. N., Thornton, J. A., Cubison, M. J., Gonin, M., and Worsnop, D. R.: A field-deployable, chemical ionization time-of-flight mass spectrometer, *Atmospheric Measurement Techniques*, 4, 1471–1479, <https://doi.org/10.5194/amt-4-1471-2011>, 2011.
- 615
- Brühl, C., Lelieveld, J., Crutzen, P. J., and Tost, H.: The role of carbonyl sulphide as a source of stratospheric sulphate aerosol and its impact on climate, *Atmospheric Chemistry and Physics*, 12, 1239–1253, <https://doi.org/10.5194/acp-12-1239-2012>, 2012.
- Burkholder, J. B., Sander, S. P., Abbatt, J., Barker, J. R., Cappa, C., Crouse, J. D., Dibble, T. S., Huie, R. E., Kolb, C. E., Kurylo, M. J., Orkin, V. L., Percival, C. J., Wilmouth, D. M., and Wine, P. H.: Chemical Kinetics and Photochemical Data for Use in Atmospheric Studies, Evaluation No. 19, JPL Publication 19-5, <http://jpldataeval.jpl.nasa.gov>, 2019.
- 620
- Challenger, F. and Simpson, M. I.: 320. Studies on biological methylation. Part XII. A precursor of the dimethyl sulphide evolved by *Polysiphonia fastigiata*. dimethyl-2-carboxyethylsulphonium hydroxide and its salts, *J. Chem. Soc.*, 1591, <https://doi.org/10.1039/jr9480001591>, 1948.
- Chan, Y.-C., Evans, M. J., He, P., Holmes, C. D., Jaeglé, L., Kasibhatla, P., Liu, X.-Y., Sherwen, T., Thornton, J. A., Wang, X., Xie, Z., Zhai, S., and Alexander, B.: Heterogeneous Nitrate Production Mechanisms in Intense Haze Events in the North China Plain, *Journal of Geophysical Research: Atmospheres*, 126, e2021JD034688, <https://doi.org/10.1029/2021JD034688>, 2021.
- 625



- Chen, J., Lane, J. R., Bates, K. H., and Kjaergaard, H. G.: Atmospheric Gas-Phase Formation of Methanesulfonic Acid, *Environ. Sci. Technol.*, 57, 21168–21177, <https://doi.org/10.1021/acs.est.3c07120>, 2023.
- 630 Chen, Q., Sherwen, T., Evans, M., and Alexander, B.: DMS oxidation and sulfur aerosol formation in the marine troposphere: a focus on reactive halogen and multiphase chemistry, *Atmos. Chem. Phys.*, 18, 13617–13637, <https://doi.org/10.5194/acp-18-13617-2018>, 2018.
- Chernykh, I. V. and Eskridge, R. E.: Determination of Cloud Amount and Level from Radiosonde Soundings, *Journal of Applied Meteorology and Climatology*, 35, 1362–1369, [https://doi.org/10.1175/1520-0450\(1996\)035<1362:DOCAAL>2.0.CO;2](https://doi.org/10.1175/1520-0450(1996)035<1362:DOCAAL>2.0.CO;2), 1996.
- 635
- Chin, M., Jacob, D. J., Gardner, G. M., Foreman-Fowler, M. S., Spiro, P. A., and Savoie, D. L.: A global three-dimensional model of tropospheric sulfate, *Journal of Geophysical Research: Atmospheres*, 101, 18667–18690, <https://doi.org/10.1029/96JD01221>, 1996.
- Conley, S. A., Faloon, I., Miller, G. H., Lenschow, D. H., Blomquist, B., and Bandy, A.: Closing the dimethyl sulfide budget in the tropical marine boundary layer during the Pacific Atmospheric Sulfur Experiment, *Atmospheric Chemistry and Physics*, 9, 8745–8756, <https://doi.org/10.5194/acp-9-8745-2009>, 2009.
- 640
- Covert, D. S., Kapustin, V. N., Quinn, P. K., and Bates, T. S.: New particle formation in the marine boundary layer, *Journal of Geophysical Research: Atmospheres*, 97, 20581–20589, <https://doi.org/10.1029/92JD02074>, 1992.
- Creasey, D. J., Evans, G. E., Heard, D. E., and Lee, J. D.: Measurements of OH and HO₂ concentrations in the Southern Ocean marine boundary layer, *Journal of Geophysical Research: Atmospheres*, 108, <https://doi.org/10.1029/2002JD003206>, 2003.
- 645
- De Bruyn, W. J., Zahniser, M. S., and Kolb, C. E.: Uptake of gas phase sulfur species methanesulfonic acid, dimethylsulfoxide, and dimethyl sulfone by aqueous surfaces, *Journal of Geophysical Research: Atmospheres*, 99, 16927–16932, <https://doi.org/10.1029/94JD00684>, 1994.
- Faloon, I.: Sulfur processing in the marine atmospheric boundary layer: A review and critical assessment of modeling uncertainties, *Atmospheric Environment*, 43, 2841–2854, <https://doi.org/10.1016/j.atmosenv.2009.02.043>, 2009.
- 650
- Feingold, G., Kreidenweis, S. M., and Zhang, Y.: Stratocumulus processing of gases and cloud condensation nuclei: 1. Trajectory ensemble model, *Journal of Geophysical Research: Atmospheres*, 103, 19527–19542, <https://doi.org/10.1029/98JD01750>, 1998.
- Feingold, G., McComiskey, A., Rosenfeld, D., and Sorooshian, A.: On the relationship between cloud contact time and precipitation susceptibility to aerosol, *Journal of Geophysical Research: Atmospheres*, 118, 10,544–10,554, <https://doi.org/10.1002/jgrd.50819>, 2013.
- 655
- Flynn, D. and Morris, V.: Total Sky Imager (TSISKYCOVER), <http://dx.doi.org/10.5439/1992207>, 2022.
- Gelaro, R., McCarty, W., Suárez, M. J., Todling, R., Molod, A., Takacs, L., Randles, C. A., Darmenov, A., Bosilovich, M. G., Reichle, R., Wargan, K., Coy, L., Cullather, R., Draper, C., Akella, S., Buchard, V., Conaty, A., Silva, A. M. da, Gu, W., Kim, G.-K., Koster, R., Lucchesi, R., Merkova, D., Nielsen, J. E., Partyka, G., Pawson, S., Putman, W., Rienecker, M., Schubert, S. D., Sienkiewicz, M., and Zhao, B.: The Modern-Era Retrospective Analysis for Research and Applications, Version 2 (MERRA-2), *Journal of Climate*, 30, 5419–5454, <https://doi.org/10.1175/JCLI-D-16-0758.1>, 2017.
- 660



- 665 Ghate, V. P., Surlleta, T., Magaritz-Ronen, L., Raveh-Rubin, S., Gallo, F., Carlton, A. G., and Azevedo, E. B.: Drivers of Cloud Condensation Nuclei in the Eastern North Atlantic as Observed at the ARM Site, *Journal of Geophysical Research: Atmospheres*, 128, e2023JD038636, <https://doi.org/10.1029/2023JD038636>, 2023.
- Global Modeling and Assimilation Office (GMAO): MERRA-2 tavg3_3d_rad_Np: 3d,3-Hourly,Time-Averaged,Pressure-Level,Assimilation,Radiation Diagnostics V5.12.4, <https://doi.org/10.5067/3UG8WQXZAOK>, 2015.
- 670 Hall, S. R., Ullmann, K., Prather, M. J., Flynn, C. M., Murray, L. T., Fiore, A. M., Correa, G., Strode, S. A., Steenrod, S. D., Lamarque, J.-F., Guth, J., Josse, B., Flemming, J., Huijnen, V., Abraham, N. L., and Archibald, A. T.: Cloud impacts on photochemistry: building a climatology of photolysis rates from the Atmospheric Tomography mission, *Atmospheric Chemistry and Physics*, 18, 16809–16828, <https://doi.org/10.5194/acp-18-16809-2018>, 2018.
- Heffter, J.: Transport Layer Depth Calculations, Second Joint Conference on Applications of Air Pollution Meteorology, New Orleans, Louisiana, 1980.
- 675 Hoffmann, E. H., Tilgner, A., Schrödner, R., Bräuer, P., Wolke, R., and Herrmann, H.: An advanced modeling study on the impacts and atmospheric implications of multiphase dimethyl sulfide chemistry, *Proc Natl Acad Sci USA*, 113, 11776–11781, <https://doi.org/10.1073/pnas.1606320113>, 2016.
- Hoffmann, E. H., Heinold, B., Kubin, A., Tegen, I., and Herrmann, H.: The Importance of the Representation of DMS Oxidation in Global Chemistry-Climate Simulations, *Geophysical Research Letters*, 48, e2021GL094068, <https://doi.org/10.1029/2021GL094068>, 2021.
- 680 Holmes, C. D.: Technical note: Entrainment-limited kinetics of bimolecular reactions in clouds, *Atmospheric Chemistry and Physics*, 22, 9011–9015, <https://doi.org/10.5194/acp-22-9011-2022>, 2022.
- Holmes, C. D., Bertram, T. H., Confer, K. L., Graham, K. A., Ronan, A. C., Wirks, C. K., and Shah, V.: The Role of Clouds in the Tropospheric NO_x Cycle: A New Modeling Approach for Cloud Chemistry and Its Global Implications, *Geophysical Research Letters*, 46, 4980–4990, <https://doi.org/10.1029/2019GL081990>, 2019.
- 685 Hulswar, S., Simó, R., Galí, M., Bell, T. G., Lana, A., Inamdar, S., Halloran, P. R., Manville, G., and Mahajan, A. S.: Third revision of the global surface seawater dimethyl sulfide climatology (DMS-Rev3), *Earth System Science Data*, 14, 2963–2987, <https://doi.org/10.5194/essd-14-2963-2022>, 2022.
- Irwin, J. G. and Williams, M. L.: Acid rain: Chemistry and transport, *Environmental Pollution*, 50, 29–59, [https://doi.org/10.1016/0269-7491\(88\)90184-4](https://doi.org/10.1016/0269-7491(88)90184-4), 1988.
- 690 Iyer, S., Lopez-Hilfiker, F., Lee, B. H., Thornton, J. A., and Kurtén, T.: Modeling the Detection of Organic and Inorganic Compounds Using Iodide-Based Chemical Ionization, *J. Phys. Chem. A*, 120, 576–587, <https://doi.org/10.1021/acs.jpca.5b09837>, 2016.
- Jenkin, M. E., Saunders, S. M., and Pilling, M. J.: The tropospheric degradation of volatile organic compounds: a protocol for mechanism development, *Atmospheric Environment*, 31, 81–104, [https://doi.org/10.1016/S1352-2310\(96\)00105-7](https://doi.org/10.1016/S1352-2310(96)00105-7), 1997.
- 695 Jernigan, C. M., Fite, C. H., Vereecken, L., Berkelhammer, M. B., Rollins, A. W., Rickly, P. S., Novelli, A., Taraborrelli, D., Holmes, C. D., and Bertram, T. H.: Efficient Production of Carbonyl Sulfide in the Low-NO_x Oxidation of Dimethyl Sulfide, *Geophysical Research Letters*, 49, e2021GL096838, <https://doi.org/10.1029/2021GL096838>, 2022a.
- Jernigan, C. M., Cappa, C. D., and Bertram, T. H.: Reactive Uptake of Hydroperoxymethyl Thioformate to Sodium Chloride and Sodium Iodide Aerosol Particles, *J. Phys. Chem. A*, 126, 4476–4481, <https://doi.org/10.1021/acs.jpca.2c03222>, 2022b.



- 700 Jernigan, C. M., Rivard, M. J., Berkelhammer, M. B., and Bertram, T. H.: Sulfate and Carbonyl Sulfide Production in Aqueous Reactions of Hydroperoxymethyl Thioformate, ACS EST Air, <https://doi.org/10.1021/acsestair.3c00098>, 2024.
- Johnson, K., Giangrande, S., and Toto, T.: Active Remote Sensing of Clouds (ARSCL) product using Ka-band ARM Zenith Radars (ARSCLKAZRBND1KOLLISAS), <http://dx.doi.org/10.5439/1393438>, 2022.
- 705 Johnson, M. T.: A numerical scheme to calculate temperature and salinity dependent air-water transfer velocities for any gas, Ocean Sci., 6, 913–932, <https://doi.org/10.5194/os-6-913-2010>, 2010.
- Jokinen, T., Sipilä, M., Kontkanen, J., Vakkari, V., Tisler, P., Duplissy, E.-M., Junninen, H., Kangasluoma, J., Manninen, H. E., Petäjä, T., Kulmala, M., Worsnop, D. R., Kirkby, J., Virkkula, A., and Kerminen, V.-M.: Ion-induced sulfuric acid–ammonia nucleation drives particle formation in coastal Antarctica, Science Advances, 4, eaat9744, <https://doi.org/10.1126/sciadv.aat9744>, 2018.
- 710 Khan, M. A. H., Bannan, T. J., Holland, R., Shallcross, D. E., Archibald, A. T., Matthews, E., Back, A., Allan, J., Coe, H., Artaxo, P., and Percival, C. J.: Impacts of Hydroperoxymethyl Thioformate on the Global Marine Sulfur Budget, ACS Earth Space Chem., 5, 2577–2586, <https://doi.org/10.1021/acsearthspacechem.1c00218>, 2021.
- Kiene, R. P.: Production of methanethiol from dimethylsulfoniopropionate in marine surface waters, Marine Chemistry, 54, 69–83, [https://doi.org/10.1016/0304-4203\(96\)00006-0](https://doi.org/10.1016/0304-4203(96)00006-0), 1996.
- 715 Kilgour, D. B. and Bertram, T. H.: Cloud processing of DMS oxidation products limits SO₂ and OCS production in the Eastern North Atlantic marine boundary layer, MINDS@UW [data set], <http://digital.library.wisc.edu/1793/85493>, 2024.
- Kilgour, D. B., Novak, G. A., Sauer, J. S., Moore, A. N., Dinasquet, J., Amiri, S., Franklin, E. B., Mayer, K., Winter, M., Morris, C. K., Price, T., Malfatti, F., Crocker, D. R., Lee, C., Cappa, C. D., Goldstein, A. H., Prather, K. A., and Bertram, T. H.: Marine gas-phase sulfur emissions during an induced phytoplankton bloom, Atmospheric Chemistry and Physics, 22, 1601–1613, <https://doi.org/10.5194/acp-22-1601-2022>, 2022.
- 720 Kilgour, D. B., Jernigan, C. M., Zhou, S., Brito de Azevedo, E., Wang, J., Zawadowicz, M. A., and Bertram, T. H.: Contribution of Speciated Monoterpenes to Secondary Aerosol in the Eastern North Atlantic, ACS EST Air, <https://doi.org/10.1021/acsestair.3c00112>, 2024.
- 725 Kogan, Y. L.: Large-Eddy Simulation of Air Parcels in Stratocumulus Clouds: Time Scales and Spatial Variability, Journal of the Atmospheric Sciences, 63, 952–967, <https://doi.org/10.1175/JAS3665.1>, 2006.
- Krechmer, J., Lopez-Hilfiker, F., Koss, A., Hutterli, M., Stoermer, C., Deming, B., Kimmel, J., Warneke, C., Holzinger, R., Jayne, J., Worsnop, D., Fuhrer, K., Gonin, M., and de Gouw, J.: Evaluation of a New Reagent-Ion Source and Focusing Ion–Molecule Reactor for Use in Proton-Transfer-Reaction Mass Spectrometry, Anal. Chem., 90, 12011–12018, <https://doi.org/10.1021/acs.analchem.8b02641>, 2018.
- 730 Kremser, S., Thomason, L. W., von Hobe, M., Hermann, M., Deshler, T., Timmreck, C., Toohey, M., Stenke, A., Schwarz, J. P., Weigel, R., Fueglistaler, S., Prata, F. J., Vernier, J.-P., Schlager, H., Barnes, J. E., Antuña-Marrero, J.-C., Fairlie, D., Palm, M., Mahieu, E., Notholt, J., Rex, M., Bingen, C., Vanhellemont, F., Bourassa, A., Plane, J. M. C., Klocke, D., Carn, S. A., Clarisse, L., Trickl, T., Neely, R., James, A. D., Rieger, L., Wilson, J. C., and Meland, B.: Stratospheric aerosol—Observations, processes, and impact on climate, Reviews of Geophysics, 54, 278–335, <https://doi.org/10.1002/2015RG000511>, 2016.
- 735 Kuma, P., McDonald, A. J., Morgenstern, O., Alexander, S. P., Cassano, J. J., Garrett, S., Halla, J., Hartery, S., Harvey, M. J., Parsons, S., Plank, G., Varma, V., and Williams, J.: Evaluation of Southern Ocean cloud in the HadGEM3 general circulation



model and MERRA-2 reanalysis using ship-based observations, *Atmospheric Chemistry and Physics*, 20, 6607–6630, <https://doi.org/10.5194/acp-20-6607-2020>, 2020.

740 Lamkaddam, H., Dommen, J., Ranjithkumar, A., Gordon, H., Wehrle, G., Krechmer, J., Majluf, F., Salionov, D., Schmale, J., Bjelić, S., Carslaw, K. S., El Haddad, I., and Baltensperger, U.: Large contribution to secondary organic aerosol from isoprene cloud chemistry, *Science Advances*, 7, eabe2952, <https://doi.org/10.1126/sciadv.abe2952>, 2021.

Lawson, S. J., Law, C. S., Harvey, M. J., Bell, T. G., Walker, C. F., de Bruyn, W. J., and Saltzman, E. S.: Methanethiol, dimethyl sulfide and acetone over biologically productive waters in the southwest Pacific Ocean, *Atmos. Chem. Phys.*, 18, 2020.

745 Lee, J. D., Moller, S. J., Read, K. A., Lewis, A. C., Mendes, L., and Carpenter, L. J.: Year-round measurements of nitrogen oxides and ozone in the tropical North Atlantic marine boundary layer, *Journal of Geophysical Research: Atmospheres*, 114, <https://doi.org/10.1029/2009JD011878>, 2009.

Levine, S. Z. and Schwartz, S. E.: In-cloud and below-cloud scavenging of Nitric acid vapor, *Atmospheric Environment* (1967), 16, 1725–1734, [https://doi.org/10.1016/0004-6981\(82\)90266-9](https://doi.org/10.1016/0004-6981(82)90266-9), 1982.

750 Li, Y., Barth, M. C., Patton, E. G., and Steiner, A. L.: Impact of In-Cloud Aqueous Processes on the Chemistry and Transport of Biogenic Volatile Organic Compounds, *Journal of Geophysical Research: Atmospheres*, 122, 11,131–11,153, <https://doi.org/10.1002/2017JD026688>, 2017.

Liggio, J. and Li, S.-M.: Reactive uptake of pinonaldehyde on acidic aerosols, *Journal of Geophysical Research: Atmospheres*, 111, <https://doi.org/10.1029/2005JD006978>, 2006.

755 Montzka, S. A., Calvert, P., Hall, B. D., Elkins, J. W., Conway, T. J., Tans, P. P., and Sweeney, C.: On the global distribution, seasonality, and budget of atmospheric carbonyl sulfide (COS) and some similarities to CO₂, *Journal of Geophysical Research: Atmospheres*, 112, <https://doi.org/10.1029/2006JD007665>, 2007.

760 Naud, C. M., Elsaesser, G. S., and Booth, J. F.: Dominant Cloud Controlling Factors for Low-Level Cloud Fraction: Subtropical Versus Extratropical Oceans, *Geophysical Research Letters*, 50, e2023GL104496, <https://doi.org/10.1029/2023GL104496>, 2023.

NOAA National Centers for Environmental Information: GOES-R Algorithm working Group, and GOES-R Series Program: NOAA GOES-R Series Advanced Baseline Imager (ABI) Level 2 Cloud and Moisture Imagery Products (CMIP). MCMIPF., <https://doi.org/doi:10.7289/V5736P36>, 2017.

765 Novak, G. A., Fite, C. H., Holmes, C. D., Veres, P. R., Neuman, J. A., Faloona, I., Thornton, J. A., Wolfe, G. M., Vermeuel, M. P., Jernigan, C. M., Peischl, J., Ryerson, T. B., Thompson, C. R., Bourgeois, I., Warneke, C., Gkatzelis, G. I., Coggon, M. M., Sekimoto, K., Bui, T. P., Dean-Day, J., Diskin, G. S., DiGangi, J. P., Nowak, J. B., Moore, R. H., Wiggins, E. B., Winstead, E. L., Robinson, C., Thornhill, K. L., Sanchez, K. J., Hall, S. R., Ullmann, K., Dollner, M., Weinzierl, B., Blake, D. R., and Bertram, T. H.: Rapid cloud removal of dimethyl sulfide oxidation products limits SO₂ and cloud condensation nuclei production in the marine atmosphere, *Proc. Natl. Acad. Sci. U.S.A.*, 118, e2110472118, <https://doi.org/10.1073/pnas.2110472118>, 2021.

770 Novak, G. A., Kilgour, D. B., Jernigan, C. M., Vermeuel, M. P., and Bertram, T. H.: Oceanic emissions of dimethyl sulfide and methanethiol and their contribution to sulfur dioxide production in the marine atmosphere, *Atmos. Chem. Phys.*, 22, 6309–6325, <https://doi.org/10.5194/acp-22-6309-2022>, 2022.



- 775 Parrella, J. P., Jacob, D. J., Liang, Q., Zhang, Y., Mickley, L. J., Miller, B., Evans, M. J., Yang, X., Pyle, J. A., Theys, N., and Van Roozendaal, M.: Tropospheric bromine chemistry: implications for present and pre-industrial ozone and mercury, *Atmospheric Chemistry and Physics*, 12, 6723–6740, <https://doi.org/10.5194/acp-12-6723-2012>, 2012.
- Podglajen, A., Plougonven, R., Hertzog, A., and Legras, B.: A modelling case study of a large-scale cirrus in the tropical tropopause layer, *Atmospheric Chemistry and Physics*, 16, 3881–3902, <https://doi.org/10.5194/acp-16-3881-2016>, 2016.
- 780 Riihimäki, L., Sivaraman, C., and Zhang, D.: Planetary Boundary Layer Height (PBLHTSONDE1MCFARL), <http://dx.doi.org/10.5439/1991783>, 2022.
- Riva, M., Pospisilova, V., Frege, C., Perrier, S., Bansal, P., Jorga, S., Sturm, P., Thornton, J., Rohner, U., and Lopez-Hilfiker, F.: Evaluation of a reduced pressure chemical ion reactor utilizing adduct ionization for the detection of gaseous organic and inorganic species, *EGUsphere*, 1–33, <https://doi.org/10.5194/egusphere-2024-945>, 2024.
- 785 Saunders, S. M., Jenkin, M. E., Derwent, R. G., and Pilling, M. J.: Protocol for the development of the Master Chemical Mechanism, MCM v3 (Part A): tropospheric degradation of non-aromatic volatile organic compounds, *Atmospheric Chemistry and Physics*, 3, 161–180, <https://doi.org/10.5194/acp-3-161-2003>, 2003.
- Shah, V., Jacob, D. J., Thackray, C. P., Wang, X., Sunderland, E. M., Dibble, T. S., Saiz-Lopez, A., Černušák, I., Kellö, V., Castro, P. J., Wu, R., and Wang, C.: Improved Mechanistic Model of the Atmospheric Redox Chemistry of Mercury, *Environ. Sci. Technol.*, 55, 14445–14456, <https://doi.org/10.1021/acs.est.1c03160>, 2021.
- 790 Siegel, K., Gramlich, Y., Haslett, S. L., Freitas, G., Krejci, R., Zieger, P., and Mohr, C.: Arctic observations of hydroperoxymethyl thioformate (HPMTF) – seasonal behavior and relationship to other oxidation products of dimethyl sulfide at the Zeppelin Observatory, Svalbard, *Atmospheric Chemistry and Physics*, 23, 7569–7587, <https://doi.org/10.5194/acp-23-7569-2023>, 2023.
- 795 Spivakovsky, C. M., Logan, J. A., Montzka, S. A., Balkanski, Y. J., Foreman-Fowler, M., Jones, D. B. A., Horowitz, L. W., Fusco, A. C., Brenninkmeijer, C. a. M., Prather, M. J., Wofsy, S. C., and McElroy, M. B.: Three-dimensional climatological distribution of tropospheric OH: Update and evaluation, *Journal of Geophysical Research: Atmospheres*, 105, 8931–8980, <https://doi.org/10.1029/1999JD901006>, 2000.
- 800 Stevens, B., Feingold, G., Cotton, W. R., and Walko, R. L.: Elements of the microphysical structure of numerically simulated nonprecipitating stratocumulus, *Journal of the Atmospheric Sciences*, 53, 980–1006, [https://doi.org/10.1175/1520-0469\(1996\)053<0980:EOTMSO>2.0.CO;2](https://doi.org/10.1175/1520-0469(1996)053<0980:EOTMSO>2.0.CO;2), 1996.
- Tost, H., Jöckel, P., Kerkweg, A., Sander, R., and Lelieveld, J.: Technical note: A new comprehensive SCAVenging submodel for global atmospheric chemistry modelling, *Atmospheric Chemistry and Physics*, 6, 565–574, <https://doi.org/10.5194/acp-6-565-2006>, 2006.
- 805 Uin, J., Aiken, A. C., Dubey, M. K., Kuang, C., Pekour, M., Salwen, C., Sedlacek, A. J., Senum, G., Smith, S., Wang, J., Watson, T. B., and Springston, S. R.: Atmospheric Radiation Measurement (ARM) Aerosol Observing Systems (AOS) for Surface-Based In Situ Atmospheric Aerosol and Trace Gas Measurements, *Journal of Atmospheric and Oceanic Technology*, 36, 2429–2447, <https://doi.org/10.1175/JTECH-D-19-0077.1>, 2019.
- 810 Vaughan, S., Ingham, T., Whalley, L. K., Stone, D., Evans, M. J., Read, K. A., Lee, J. D., Moller, S. J., Carpenter, L. J., Lewis, A. C., Fleming, Z. L., and Heard, D. E.: Seasonal observations of OH and HO₂ in the remote tropical marine boundary layer, *Atmospheric Chemistry and Physics*, 12, 2149–2172, <https://doi.org/10.5194/acp-12-2149-2012>, 2012.



- 815 Veres, P. R., Neuman, J. A., Bertram, T. H., Assaf, E., Wolfe, G. M., Williamson, C. J., Weinzierl, B., Tilmes, S., Thompson, C. R., Thames, A. B., Schroder, J. C., Saiz-Lopez, A., Rollins, A. W., Roberts, J. M., Price, D., Peischl, J., Nault, B. A., Möller, K. H., Miller, D. O., Meinardi, S., Li, Q., Lamarque, J.-F., Kupc, A., Kjaergaard, H. G., Kinnison, D., Jimenez, J. L., Jernigan, C. M., Hornbrook, R. S., Hills, A., Dollner, M., Day, D. A., Cuevas, C. A., Campuzano-Jost, P., Burkholder, J., Bui, T. P.,
820 Brune, W. H., Brown, S. S., Brock, C. A., Bourgeois, I., Blake, D. R., Apel, E. C., and Ryerson, T. B.: Global airborne sampling reveals a previously unobserved dimethyl sulfide oxidation mechanism in the marine atmosphere, *Proc Natl Acad Sci USA*, 201919344, <https://doi.org/10.1073/pnas.1919344117>, 2020.
- Vermeuel, M. P., Novak, G. A., Jernigan, C. M., and Bertram, T. H.: Diel Profile of Hydroperoxymethyl Thioformate: Evidence for Surface Deposition and Multiphase Chemistry, *Environ. Sci. Technol.*, 54, 12521–12529, <https://doi.org/10.1021/acs.est.0c04323>, 2020.
- Wang, X., Jacob, D. J., Downs, W., Zhai, S., Zhu, L., Shah, V., Holmes, C. D., Sherwen, T., Alexander, B., Evans, M. J., Eastham, S. D., Neuman, J. A., Veres, P. R., Koenig, T. K., Volkamer, R., Huey, L. G., Bannan, T. J., Percival, C. J., Lee, B. H., and Thornton, J. A.: Global tropospheric halogen (Cl, Br, I) chemistry and its impact on oxidants, *Atmospheric Chemistry and Physics*, 21, 13973–13996, <https://doi.org/10.5194/acp-21-13973-2021>, 2021.
- 825 Wolfe, G. M., Marvin, M. R., Roberts, S. J., Travis, K. R., and Liao, J.: The Framework for 0-D Atmospheric Modeling (F0AM) v3.1, *Geoscientific Model Development*, 9, 3309–3319, <https://doi.org/10.5194/gmd-9-3309-2016>, 2016.
- Wood, R.: Stratocumulus Clouds, *Monthly Weather Review*, 140, 2373–2423, <https://doi.org/10.1175/MWR-D-11-00121.1>, 2012.
- 830 Wu, R., Wang, S., and Wang, L.: New Mechanism for the Atmospheric Oxidation of Dimethyl Sulfide. The Importance of Intramolecular Hydrogen Shift in a CH₃SCH₂O Radical, *J. Phys. Chem. A*, 119, 112–117, <https://doi.org/10.1021/jp511616j>, 2015.
- Yang, Q., Easter, R. C., Campuzano-Jost, P., Jimenez, J. L., Fast, J. D., Ghan, S. J., Wang, H., Berg, L. K., Barth, M. C., Liu, Y., Shrivastava, M. B., Singh, B., Morrison, H., Fan, J., Ziegler, C. L., Bela, M., Apel, E., Diskin, G. S., Mikoviny, T., and Wisthaler, A.: Aerosol transport and wet scavenging in deep convective clouds: A case study and model evaluation using a multiple passive tracer analysis approach, *Journal of Geophysical Research: Atmospheres*, 120, 8448–8468, <https://doi.org/10.1002/2015JD023647>, 2015.
- 835 Zhang, X., Massoli, P., Quinn, P. K., Bates, T. S., and Cappa, C. D.: Hygroscopic growth of submicron and supermicron aerosols in the marine boundary layer, *Journal of Geophysical Research: Atmospheres*, 119, 8384–8399, <https://doi.org/10.1002/2013JD021213>, 2014.
- 840 Zieger, P., Väisänen, O., Corbin, J. C., Partridge, D. G., Bastelberger, S., Mousavi-Fard, M., Rosati, B., Gysel, M., Krieger, U. K., Leck, C., Nenes, A., Riipinen, I., Virtanen, A., and Salter, M. E.: Revising the hygroscopicity of inorganic sea salt particles, *Nat Commun*, 8, 15883, <https://doi.org/10.1038/ncomms15883>, 2017.